Regionally coupled atmosphere-ocean-sea ice-marine biogeochemistry model ROM: 1. Description and validation

AGU PUBLICATIONS

Journal of Advances in Modeling Earth Systems

RESEARCH ARTICLE
10.1002/2014MS000357

Regionally coupled atmosphere-ocean-sea ice-marine biogeochemistry model ROM: 1. Description and validation

Dmitry V. Sein[1], Uwe Mikolajewicz[2], Matthias Gröger[3], Irina Fast[4], William Cabos[5], Joaquim G. Pinto[6,7], Stefan Hagemann[2], Tido Semmler[1], Alfredo Izquierdo[8], and Daniela Jacob[9]

[1]Alfred Wegener Institute, Bremerhaven, Germany, [2]Max Planck Institute for Meteorology, Hamburg, Germany, [3]Swedish Meteorological and Hydrological Institute, Norrköping, Sweden, [4]German Climate Computing Center, Hamburg, Germany, [5]Department of Physics, University of Alcala, Madrid, Spain, [6]Department of Meteorology, University of Reading, Reading, UK, [7]Institute for Geophysics and Meteorology, University of Cologne, Cologne, Germany, [8]University of Cadiz, Marine Science and Technological Center of Andalusia, Cadiz, Spain, [9]Climate Service Center 2.0, Hamburg, Germany

Key Points:
- The regionally coupled climate model is validated for the North Atlantic
- Ocean circulation and biogeochemistry in the northern North Atlantic
- Atmospheric circulation and river runoff in Europe

Correspondence to:
D. V. Sein,
dmitry.sein@awi.de

Citation:
Sein, D. V., U. Mikolajewicz, M. Gröger, I. Fast, W. Cabos, J. G. Pinto, S. Hagemann, T. Semmler, A. Izquierdo, and D. Jacob (2015), Regionally coupled atmosphere-ocean-sea ice-marine biogeochemistry model ROM: 1. Description and validation, *J. Adv. Model. Earth Syst.*, *7*, 268–304, doi:10.1002/2014MS000357.

Received 23 JUN 2014
Accepted 5 FEB 2015
Accepted article online 10 FEB 2015
Published online 7 MAR 2015

Abstract The general circulation models used to simulate global climate typically feature resolution too coarse to reproduce many smaller-scale processes, which are crucial to determining the regional responses to climate change. A novel approach to downscale climate change scenarios is presented which includes the interactions between the North Atlantic Ocean and the European shelves as well as their impact on the North Atlantic and European climate. The goal of this paper is to introduce the global ocean-regional atmosphere coupling concept and to show the potential benefits of this model system to simulate present-day climate. A global ocean-sea ice-marine biogeochemistry model (MPIOM/HAMOCC) with regionally high horizontal resolution is coupled to an atmospheric regional model (REMO) and global terrestrial hydrology model (HD) via the OASIS coupler. Moreover, results obtained with ROM using NCEP/NCAR reanalysis and ECHAM5/MPIOM CMIP3 historical simulations as boundary conditions are presented and discussed for the North Atlantic and North European region. The validation of all the model components, i.e., ocean, atmosphere, terrestrial hydrology, and ocean biogeochemistry is performed and discussed. The careful and detailed validation of ROM provides evidence that the proposed model system improves the simulation of many aspects of the regional climate, remarkably the ocean, even though some biases persist in other model components, thus leaving potential for future improvement. We conclude that ROM is a powerful tool to estimate possible impacts of climate change on the regional scale.

1. Introduction

Numerical models are very effective tools to investigate the complex systems and associated mechanisms in climate and environmental sciences. Recently, much effort has been made to develop Earth System Models (ESMs) that include coupled representations of the ocean, atmosphere, land use, vegetation, biogeochemistry, atmospheric chemistry, and the hydrological cycle [*Taylor et al.*, 2012]. ESMs can be used to simulate not only the longer-term evolution of the Earth's climate on decadal and longer time scales but also to make short and medium-range weather forecasts and seasonal predictions. Still, ESMs have difficulties simulating weather and climate on regional and local scales. For example, limitations in computer power do not allow simulations with sufficient horizontal resolution to resolve key processes necessary for those spatial scales. The application of regional climate models (RCMs) is a valid possibility to improve on this drawback of current ESMs. RCMs take the initial conditions, time-dependent lateral conditions, and surface boundary conditions from the global models and provide dynamically downscaled climate information within the region of interest. Additionally, they allow a better understanding of various aspects of air-sea interaction processes important for the climate.

There is a vigorous ongoing debate on whether RCMs can provide added value to GCMs in the context of determining the regional responses to climate change. This discussion relates primarily to the fact that climate is by its nature a large-scale phenomenon. Large-scale phenomena like the Inter Tropical Convergence Zone (ITCZ) or the monsoon circulation in the subtropics, or large-scale patterns of variability such as the North Atlantic Oscillation [*Hurrell and Deser*, 2009], are reproduced reasonably well in global climate models. The spatial extension of these phenomena and patterns is in most cases larger than the domain size of

most RCMs. Historically, RCMs have been developed primarily to reproduce an observed climatology rather than to predict the regional responses to a changing climate [e.g., *Kerr*, 2013]. Still, *Feser et al*. [2011] could demonstrate an added value by analyzing different regional atmospheric models for reanalysis hindcast simulations and simulations driven by climate model output. The added value originates mainly from the higher-resolved orography in the RCMs, and the added value is larger for parameters exhibiting high spatial variability, such as near-surface temperature [*Feser et al*., 2011].

To date, many RCMs have been composed of an atmospheric component coupled to a land surface scheme and driven over ocean areas by prescribed sea surface temperature (SST) and sea ice cover. Although these RCMs are sufficient for many applications, there are cases when fine-scale atmosphere-ocean feedbacks can substantially influence the spatial and temporal structure of regional climate [*Li et al*., 2012]. Recent studies have shown that regional atmosphere-ocean climate models (RAOCMs) are capable of simulating these features of the climate system. For instance, *Ratnam et al*. [2008] found that coupling considerably improved the simulation of the Indian monsoon rain band over both the ocean and land areas. A similar result has been obtained by *Li and Zhou* [2010] in the simulation of East Asia monsoon precipitation. *Aldrian et al*. [2005] have shown that interactive calculation of SST with high spatial resolution leads to a significant improvement of the simulation of rainfall over Indonesia. Recently, a number of RAOCMs have been developed for studying the climate in the Mediterranean region, characterized by a complex morphology and strong air-sea interactions. *Somot et al*. [2008] coupled the global atmospheric model ARPEGE [*Déqué and Piedelievre*, 1995] with the regional ocean model OPAMED [*Somot et al*., 2006] and studied the climate change signal in the Mediterranean. A similar development was conducted by *Artale et al*. [2009] with the PROTHEUS system, an atmosphere-ocean RCM for the Mediterranean basin. *Dobrinski et al*. [2012] developed MORCE (Model of the Regional Coupled Earth system), a coupled ocean-atmosphere with nonhydrostatic capabilities. Several regional coupled model systems have been developed to study interannual variability in the Arctic [e.g., *Döscher et al*., 2002; *Rinke et al*., 2003; *Mikolajewicz et al*., 2005; *Sein et al*., 2014].

Compared to global coupled atmosphere-ocean models, RAOCMs can achieve much higher resolution and detailed parameterizations, providing a more accurate representation of the morphological complexity of the land-sea contrasts and relevant small-scale processes. Compared to atmosphere and ocean only regional models, RAOCMs also give a dynamically and thermodynamically consistent representation of the SST, making the representation of interactions between the ocean and atmosphere more realistic than in atmosphere and ocean only regional models.

The development of RAOCMs can be traced back to the 1980s, when *Zebiak and Cane* [1987] coupled a Gill-type atmospheric model to a 1.5-layer oceanic model to study the ENSO phenomenon. Further evolution of regional coupled modeling progressed into two different directions. The first kind of coupled models focuses on short time scales [e.g., *Pullen et al*., 2006; *Nicholls and Toumi*, 2013; *Sanna et al*., 2013]. Models of the second group (to which the RAOCM presented here belongs) are dedicated to the simulation of regional climate on time scales from several years to several decades. To our knowledge, the first fully coupled regional atmosphere/ocean/ice models for multiyear climate simulations were developed to simulate the Baltic Sea climate by *Döscher et al*. [2002] and *Lehmann et al*. [2004]. A more complete review of previous efforts in regional climate modeling can be found in, e.g., *Seo et al*. [2007].

Here we introduce a novel approach to downscale climate simulations and to investigate the interactions between the North Atlantic and Arctic Ocean as well as the impact of ocean-atmosphere interaction processes on the regional climate. A global ocean-sea ice-marine biogeochemistry model with regionally high horizontal resolution is coupled to an atmospheric regional model and global terrestrial hydrology model. This technique of coupling divides global ocean model setup into two different subdomains: coupled, where the ocean and the atmosphere are interacting, and uncoupled, where the ocean model is driven by prescribed atmospheric forcing and runs in a so-called stand-alone mode. Therefore, choosing a specific area for the regional atmosphere we can assume that in that area the ocean-atmosphere system is "free," whereas in the remaining areas the ocean circulation is driven by prescribed atmospheric forcing.

One of the main problems of RAOCMs is the prescription of lateral boundary conditions for the regional ocean models. Currently, global ocean reanalysis data sets (e.g., SODA [*Carton and Giese*, 2008], ECCO [*Chen et al*., 2014], HYCOM [*Metzger et al*., 2014], and ORA [*Balmaseda et al*., 2013]) are available and are widely used as lateral boundary conditions for regional models; but they are mainly based on monthly means,

damping the ocean dynamics on time scales less than 1 month. Additionally, regional climate models should effectively resolve the small-scale processes that are not adequately represented in the coarser model data used as boundary conditions. This creates inconsistencies between the regional model solution and the external data that can be avoided with the consideration of a global ocean model with refined resolution within the coupled domain. The use of a global ocean model also allows trapped coastal waves (originating from outside the coupled domain) to influence the barotropic sea level variability and the bottom pressure in the coupled domain. A shortcoming of the global ocean model arises from the fact that the model is forced with low-resolution and lower-frequency atmospheric data outside the coupled region. Such atmospheric data are known to have biases, e.g., too weak wind speed in the tropics. This problem is not completely avoided by regional ocean models, because a typical ocean reanalysis which would be used as lateral boundary condition is generated by running ocean models forced by the same atmospheric reanalysis we use outside the coupled region.

Another important advantage of using a global ocean model appears when considering climate change scenario simulations for future decades. The regional ocean models have to implement lateral boundary conditions obtained from significantly coarser global AOGCMs scenario simulations, introducing biases in the results. The use of a gradually refined global ocean model coupled with a regional atmospheric model can thus provide more accurate simulations both within and outside of the coupled area. Additionally, the use of monthly mean data obtained from global AOGCM climate change scenario runs as lateral boundary condition makes the investigation of possible long-term changes in some extreme events impossible (e.g., floods in the North Sea).

The goal of this paper is to introduce the global ocean-regional atmosphere coupling concept and to demonstrate the ability of this model system to simulate present-day climate. Earlier versions of this model were used to study the effect of air-sea coupling on Indonesian rainfall [*Aldrian et al*., 2005], interannual variability of sea ice extent in the Arctic Ocean and "Nordic Seas" [*Mikolajewicz et al*., 2005], the influence of the choice of coupled area on the simulated Arctic climate [*Sein et al*., 2014], and simulation of the present climate and its future change in the region of the North Sea [*Bülow et al*., 2014; *Su et al*., 2014]. Using the global ocean model alleviates some well-known problems with oceanic boundary conditions, allows the investigation of the coupling feedbacks between coupled and uncoupled ocean areas [*Sein et al*., 2014] and provides an additional "degree of freedom" in the model setup and tuning, which can be helpful for example to adjust the ocean component for the better performance within the region of interest. For example, the better Gulf Stream separation in the uncoupled area leads to a better representation of the Subpolar Gyre (SPG), which is located in the coupled domain and plays an important role for the cyclogenesis of extratropical cyclones over the North Atlantic basin. It should be noted that the ocean model is constrained by atmospheric forcing of the driving data (in our case, reanalysis or ECHAM-MPIOM) outside the coupling area.

The paper is organized as follows. We introduce our coupled model and describe each of its components in section 2. In section 3, we present the setup of a coupled model simulation for the North Atlantic region, followed by the validation of the obtained results in section 4. Finally, section 5 gives our summary and conclusions.

2. Model Components

Our coupled model comprises the Regional atmosphere Model (REMO), the Max Planck Institute Ocean Model (MPIOM), the Hamburg Ocean Carbon Cycle (HAMOCC) model, and the Hydrological Discharge (HD) model which are coupled via OASIS coupler. Note that all models except REMO are run in a global configuration.

From now on, we use for our REMO/MPIOM/HAMOCC/HD coupled model the acronym ROM (REMO-OASIS-MPIOM).

2.1. Ocean (MPIOM)

The oceanic component of ROM is the Max Planck Institute Ocean Model (MPIOM), developed at the Max Planck Institute for Meteorology [*Marsland et al*., 2002; *Jungclaus et al*., 2013]. MPIOM is a free surface, primitive equations ocean model, which uses the Boussinesq and incompressibility approximations. The model is formulated on an orthogonal curvilinear Arakawa C-grid [*Arakawa and Lamb*, 1977] with z-level vertical

discretization. The curvilinear grid allows for the placement of the poles over land, thus removing the numerical singularity associated with convergence of meridians at the geographical North Pole. An important advantage of the curvilinear grid is that high resolution in the region of interest can be reached, while maintaining a global domain. This avoids the problems associated with either open or closed boundaries in a regional ocean model.

The model has an embedded dynamic/thermodynamic sea ice model with viscous-plastic rheology based on *Hibler* [1979]. The thermodynamics relate sea ice thickness changes to a balance of radiative, turbulent, and oceanic heat fluxes. The sea ice coverage is fractional within grid cells and is related to the thickness according to subgrid-scale parameterization of lateral versus vertical ablation and accretion following *Stössel* [1992]. The considerable insulating effects of snow accumulation on sea ice are included, along with snow-ice formation when the snow/ice interface sinks below the sea level due to snow loading.

Several parameterizations of subgrid-scale processes are incorporated in the model. First, a bottom boundary layer (BBL) slope convection scheme was included, which allows for a better representation of the flow of statically unstable dense water masses over sills and off shelves [*Marsland et al*., 2002]. Second, harmonic horizontal diffusion of the tracer fields has been replaced by an isopycnal scheme [*Griffies*, 1998]. Third, eddy-induced tracer transport has been included by the implementation of a Gent and McWilliams style parameterization [*Gent et al*., 1995]. Fourth, the deep convection is parameterized using enhanced vertical diffusion [*Marsland et al*., 2002].

The ocean tidal forcing in our model is derived from the full ephimeridic lunisolar tidal potential [*Thomas et al*., 2001]. The inclusion of the tides shortens significantly the ocean model time step. For an accurate temporal resolution of the tidal oscillations, the ocean model time step has to be limited to 15–20 min. Even if the model stability criteria allow the use of larger time steps, we have to keep in mind that for an accurate simulation of the barotropic oscillations they should be "represented" by about 50 time steps per period. In the case of coarse global climate models, this restriction could be crucial. Taking the semidiurnal tides ($\sim$12 h period) into consideration, the approximate time step in our model is about 15 min (one fiftieth of 12 h), thus satisfying this condition. As our ocean model setup has much higher spatial resolution and, the required time step is therefore much shorter, the inclusion of the ocean tides does not substantially increase computational costs.

2.2. Atmosphere (REMO)

The atmospheric component of ROM is the Regional atmosphere Model (REMO) [e.g., *Jacob*, 2001]. The dynamical core of the model as well as the discretization in space and time are based on the Europa-Model of the German Weather service [*Majewski*, 1991]. The physical parameterizations are taken from the global climate model ECHAM versions 4 and 5 [*Roeckner et al*., 1996, 2003]. REMO's prognostic variables are the surface pressure, horizontal wind components, temperature, water vapor, liquid water, and cloud ice. To avoid the largely different extensions of the grid cells close to the poles, REMO uses a rotated grid, with the equator of the rotated system in the middle of the model domain. The horizontal discretization is done on the Arakawa-C-grid and the hybrid vertical coordinates are defined according to *Simmons and Burridge* [1981]. The time discretization is based on the leap frog scheme with semiimplicit correction and Asselin filter smoothing.

For ocean grid points, sea surface temperature and sea ice distribution are prescribed as lower boundary values. The seasonally varying vegetation parameters like the vegetation ratio, the forest ratio, and leaf area index are described by *Rechid and Jacob* [2006]. All prognostic variables except for the liquid water and cloud ice are relaxed toward the forcing data in the outer eight rows of the model area according to lateral boundary conditions formulated after *Davies* [1976]. At the upper boundary, a radiative upper boundary condition following *Klemp and Durran* [1983] and *Bougeault* [1983] is applied. The radiation parameterization is adopted from the European Centre for Medium-Range Weather Forecasts' model [*Fouquart and Bonnel*, 1980; *Morcrette and Fouquart*, 1986] with changes for ECHAM4 described in *Roeckner et al*. [1996].

Clouds are divided into stratiform and convective clouds. The liquid water and ice content of stratiform clouds are determined by the corresponding budget equations, including sources and sinks due to phase changes and precipitation. The parameterizations of cloud processes are taken from the ECHAM5 model [*Roeckner et al*., 2003]. The parameterization of the convective clouds is based on the mass flux concept from *Tiedtke* [1989] with modifications of the adjustment closure for deep convection according to *Nordeng* [1994]. Soil

temperatures on land are calculated from diffusion equations solved in five different layers covering the uppermost 10 m of the soil. For the soil hydrology, three different budget equations for the amount of snow, the water intercepted by vegetation, and the soil water content are applied. The surface temperature of the sea ice is determined from the residual of the heat and radiation fluxes at the ice surface. Snow on sea ice is not explicitly considered in REMO but is indirectly accounted for by the sea ice albedo and the calculation of the conductive heat flux through the ice as an addition to the ice thickness. In our case, snow over the sea ice is accumulated and melted in MPIOM, which "receives" snow fall from REMO, and returns the effective sea ice- snow thickness and snow cover mask to REMO. The sea ice albedo is assumed to depend on the surface temperature and has values between 60% and 80%. If snow is present, this range is shifted to 65%–85%.

REMO has a fractional specification for land, water, and sea ice in one grid cell [*Semmler et al*., 2002]. At the surface, fluxes, temperature, and humidity are computed separately for each surface type, according to *Avissar and Pielke* [1989]. The surface fluxes are averaged over the three different surface types (weighted by the respective fractional area) to determine the effects of the fluxes on temperature and humidity in the lowest model level. In all other model levels, each value for the fluxes, temperature, and humidity is representative for the whole box. The model characteristics are described in more detail in *Jacob* [2001], *Jacob et al*. [2001], and *Déqué et al*. [2007].

2.3. Marine Biogeochemistry (HAMOCC)

The Hamburg Ocean Carbon Cycle model HAMOCC [*Maier-Reimer*, 1993; *Maier-Reimer et al*., 2005] includes the relevant carbon stocks of the atmosphere, the ocean, and the sediments and simulates the exchange between them. The model receives temperature and salinity fields from MPIOM to compute the transformation rate constants as required for the air-sea gas exchange, whereas tracer advection and diffusion is determined by MPIOM. Shortwave radiation at the top of the water column is given as an atmospheric forcing field to simulate photosynthesis which is limited by phosphate, nitrate, and Fe. A detailed model description and validation of the model's mean biogeochemical state is given in *Wetzel* [2004].

Modifications have been made for the current study to take the specific conditions in shallow marine semi-enclosed shelf seas into account. These comprise the implementation of a new light penetration scheme for the biogeochemical model, including light attenuation due to silt near the coasts [*Heath et al*., 2002; *Pätsch and Kühn*, 2008], and the implementation of river loads of dissolved nutrients and other chemical elements [*Meybeck and Ragu*, 1997]. Details can be found in *Gröger et al*. [2013].

HAMOCC simulates the cycle of Nutrients, Phytoplankton, Detritus, and Zooplankton (NPDZ model). It has three basic productivity limiting nutrients (PO_4, NO_3, Fe). The growth rate of phytoplankton is limited by photosynthetic active radiation, which is calculated from shortwave radiation at the surface. Light is further attenuated with depth by water turbidity and the self-shading by phytoplankton. Only one phytoplankton prognostic state variable is calculated from which opal and calcite shells are computed separately. In the global ocean, this approach reflects largely the production of Coccolithophorids, flagellates, and diatoms. The latter group is assumed to grow fastest when sufficient silicate is available. Grazing by zooplankton is modeled by a simple Monod function using a maximum growth rate (or grazing rate) and a half saturation constant. Zooplankton is further diminished by a constant death rate (parameterizing the effect of predators) and a mortality rate. The latter is immediately remineralized. Additionally, a third biomass pool of Dissolved Organic Matter (DOM) exists which is fed by phytoplankton and zooplankton excretion. Dead phytoplankton (detritus) as well as carbonate and opal shells fall down to the bottom with different constant velocities. However, aggregation processes are not accounted for. If enough oxygen and dead phytoplankton (detritus) is available, DOM is remineralized at constant rates. In the absence of oxygen, denitrification takes place by bacteria which are not modeled explicitly. Opal and carbonate shells are likewise dissolved at constant rates. The inorganic carbon cycle is represented by dissolved inorganic carbon (DIC) and total alkalinity (TA). During phytoplankton production, DIC is reduced, which lowers the air-sea pCO_2 difference at the ocean surface. Correspondingly, calcite production (dissolution) within (below) the euphotic zone reduces DIC. Thus, the model simulates the oceanic carbon pump and carbonate pump. At the bottom, the model is closed by a 12 layer sediment module [*Heinze et al*., 1999], which simulates pore water chemistry and which is in diffusive exchange with the bottom layer. The air-sea gas exchange for CO_2, O_2, and N_2 is parameterized using the Schmidt number and piston velocity according to *Wanninkhof* [1992]. The temperature dependence of the Schmidt number has been adapted according to the

recommendation of *Gröger and Mikolajewicz* [2011]. A full technical description of the model is available in *Maier-Reimer et al*. [2005].

2.4. River Runoff (HD)

The Hydrological Discharge (HD) model [*Hagemann and Dümenil*, 1998; *Hagemann and Dümenil Gates*, 2001] simulates globally the lateral freshwater fluxes at the land surface. It is a state-of-the-art discharge model that is applied and validated on the global scale, and it is also part of the coupled global AOGCM ECHAM5/MPIOM [*Roeckner et al*., 2003; *Jungclaus et al*., 2006]. As a general strategy, the HD model computes the discharge at 0.5° resolution with a daily time step. In the HD model, the lateral water flow is separated into the three flow processes: overland flow, base flow, and river flow. The overland flow uses surface runoff as input and represents the fast flow component within a grid box, the base flow is fed by drainage from the soil and represents the slow flow component, and the inflow from other grid boxes contributes to river flow. The sum of the three flow processes equals the total outflow from a grid box. The model parameters are functions of the topography gradient between grid boxes, the slope within a grid box, the grid box length, the lake area, and the wetland fraction of a particular grid box. More details can be found in model *Hagemann and Gates* [1998, 2001].

2.5. Coupling

REMO/MPIOM coupling was carried out using the OASIS coupler developed by CERFACS [*Valcke et al*., 2003]. The coupling procedure is similar to the one used in the MPI climate models ECHO-G [*Legutke and Voss*, 1999] and ECHAM5/MPIOM.

Momentum, heat, and freshwater fluxes are calculated in the atmosphere model for the open water and ice-covered part of the grid box separately:

$$Q^W = Q^W_{SW} + Q^W_{LW} + Q^W_S + Q^W_L \tag{1}$$

$$Q^I = Q^I_{SW} + Q^I_{LW} + Q^I_S + Q^I_L + Q^I_C + Q^I_R \tag{2}$$

where upper indices denote the fluxes over open water (W) and the fluxes over ice (I). Lower indices indicate net shortwave radiation (SW), net longwave radiation (LW), sensible (S) and latent (L) heat fluxes. There are two additional sources for the ice-covered part, namely the conductive heat flux ($Q^{I\,C}_C$) which is responsible for the ice growth, and the residual heat flux (Q^I_R), which is used to melt ice. Conductive heat flux through the snow/ice layer is defined as:

$$Q^I_C = \frac{k_I}{h_{eff}} \cdot (T^I - \theta)$$

where T^I is the snow/sea ice skin temperature, θ the temperature at the ice-water interface, i.e., freezing temperature, h_{eff} the effective ice thickness defined as $h_{eff} = (k_I \cdot h_S + k_S \cdot h_I)/k_S$, with k_I and k_S being the heat conductivities of ice and snow and h_I and h_S the ice and snow thickness, respectively. A detailed description of the calculation of fluxes used in (1)–(2) can be found in *Roeckner et al*. [2003] and *Legutke and Voss* [1999]

Freshwater fluxes are separated in liquid (W) and solid (I) parts:

$$P^W = P_T - P_{SN} + E^W \tag{3}$$

$$P^I = P_{SN} + E^I \tag{4}$$

where P_T is total precipitation, P_{SN} snow fall, E^W surface evaporation, and E^I sublimation of sea ice. Dynamical forcing of the ocean model is represented by wind stress and sea level pressure (SLP). Wind stress is calculated separately for open water and sea ice. We use the standard formulation of the wind stress, i.e., its quadratic dependence on the wind velocity relative to the ocean surface velocity. The difference between wind stress over sea ice and over water is given by the drag coefficient, i.e., the surface roughness. Whereas surface roughness for the open water is calculated from the Charnock formula [*Charnock*, 1955], sea ice roughness is constant and set to 1 mm in our simulations. For the partially ice-covered regions, wind stress is calculated as weighted mean of the contributions of wind stress over ice and water.

The effect of ocean surface currents is taken into account for the calculation of turbulent fluxes. The wind velocity relative to the ocean surface (sea ice) velocity $|\mathbf{W}\text{-}\mathbf{u}|$ is used, rather than the absolute near-surface

wind speed |**W**| (**u** is the ocean surface or sea ice velocity). This modification is important given strong ocean tides and in model configurations with relatively high spatial resolution [e.g., *Dawe and Thompson*, 2006], which is the case for our setup.

As the regional model (REMO) covers only a part of the global ocean, MPIOM needs to be run in both coupled (the branch REMO-OASIS-MPIOM, Figure 1) and stand-alone (the branch External Forcing-Bulk Formulae-MPIOM, Figure 1) modes simultaneously. The ocean model running in the coupled subdomain receives the heat, freshwater, and momentum fluxes calculated in REMO (F_{REMO}) at specified frequency (coupling time step) and passes the sea surface conditions to the atmospheric model. In the uncoupled subdomain, the ocean model calculates heat, freshwater, and momentum fluxes (F_{Bulk}) from the global, predefined atmospheric fields (e.g., from reanalysis data) using bulk formulas (see Figure 1 External Forcing-Bulk Formulas-MPI-OM) at specified frequency (forcing time step). A detailed description of the bulk formulas used to simulate the fluxes in the uncoupled domain can be found in *Marsland et al*. [2002]. Note that the coupled time step and the forcing time step can be different. The resulting fluxes used as ocean forcing (F_{Ocean}) are a combination of F_{REMO} and F_{Bulk}:

$$F_{Ocean} = \chi F_{REMO} + (1-\chi) F_{Bulk} \tag{5}$$

where χ is a smooth transition coefficient changing from 1 inside the REMO domain to 0 outside. The fluxes F_{REMO} are calculated in the atmospheric model according to equations (1)–(4).

Interpolation from the atmospheric grid to the ocean grid and vice versa is done in the ocean model using the so-called mosaic approach, which can be briefly described as follows:

$$F_{ij}^{MPIOM} = \frac{\sum_{lm} F_{lm}^{REMO} \cdot A_{ijlm}}{\sum_{lm} A_{ijlm}}; \quad F_{lm}^{REMO} = \frac{\sum_{ij} F_{ij}^{MPIOM} \cdot A_{ijlm}}{\sum_{ij} A_{ijlm}} \tag{6}$$

where F_{ij}^{MPIOM} and F_{lm}^{REMO} are the values of F in the ocean grid box (i,j) and atmosphere grid box (l,m), respectively. A_{ijlm} is interpolation (weight) matrix, defined as a common surface area between ocean grid box (i,j) and atmosphere grid box (l,m).

Thus, the OASIS coupler "sees" both models on the same computational grid, i.e., REMO grid. Due to the smaller spatial scales of oceanic processes, ocean models usually have a higher spatial resolution than atmospheric models. To provide the adequate atmospheric feedback for small-scale SST anomalies, a subscale correction of the atmospheric heat fluxes is applied. As these fluxes strongly depend on sea surface temperature (SST), this correction is assumed to be proportional to the difference between the SST calculated in MPI-OM and the same SST interpolated onto the atmospheric grid and backward. The proportionality constant which is equal to $\partial Q/\partial T$, where Q is a heat flux and T is a sea surface temperature, was set according to *Roeske* [2001] to 30 W/(m^2 K). Note that the value of 30 W/(m^2 K) is obtained for the northern North Atlantic. For different ocean regions, its annual mean varies from $\sim$20 W/(m^2 K) in polar regions to $\sim$65 W/(m^{2}K) in tropics [*Roeske*, 2001]. Sensitivity studies with $\partial Q/\partial T$ set to 20 and 40 W/(m^{2}K) showed that the differences to the results obtained with 30 W/(m^{2}K) were negligible. Because both the SST interpolations (forward and backward) are linear (see equation (6)), and subscale heat flux correction linearly depends on SST, the mean subscale heat correction over the coupled domain is zero. In other words, this term only redistributes atmospheric heat over smaller ocean grid cells but does not change the integrated heat balance.

REMO requires surface temperature not only over the sea, ice, or land, but also over inland lakes, which are not represented in the ocean model. Lake surface temperature (LST) is calculated using the following simplified procedure: all lakes are assumed to be well mixed and to have constant depth of 20 m. The atmospheric heat fluxes over the water in the grid box, where lakes are present, are added to the lake's heat content. If the resulting heat content is positive the lake temperature (which is assumed to be equal to the LST) is calculated from its value. If heat content becomes negative it is set to zero and the energy is used to form ice. In our model, we do not consider the case when all water of the lake is frozen. However, this possibility is not realistic under present climate conditions for a 20 m lake depth.

The Hydrological Discharge model is coupled to both the ocean and the atmosphere model with 24 h frequency. It receives the surface runoff and drainage from REMO and delivers the freshwater river inflow to

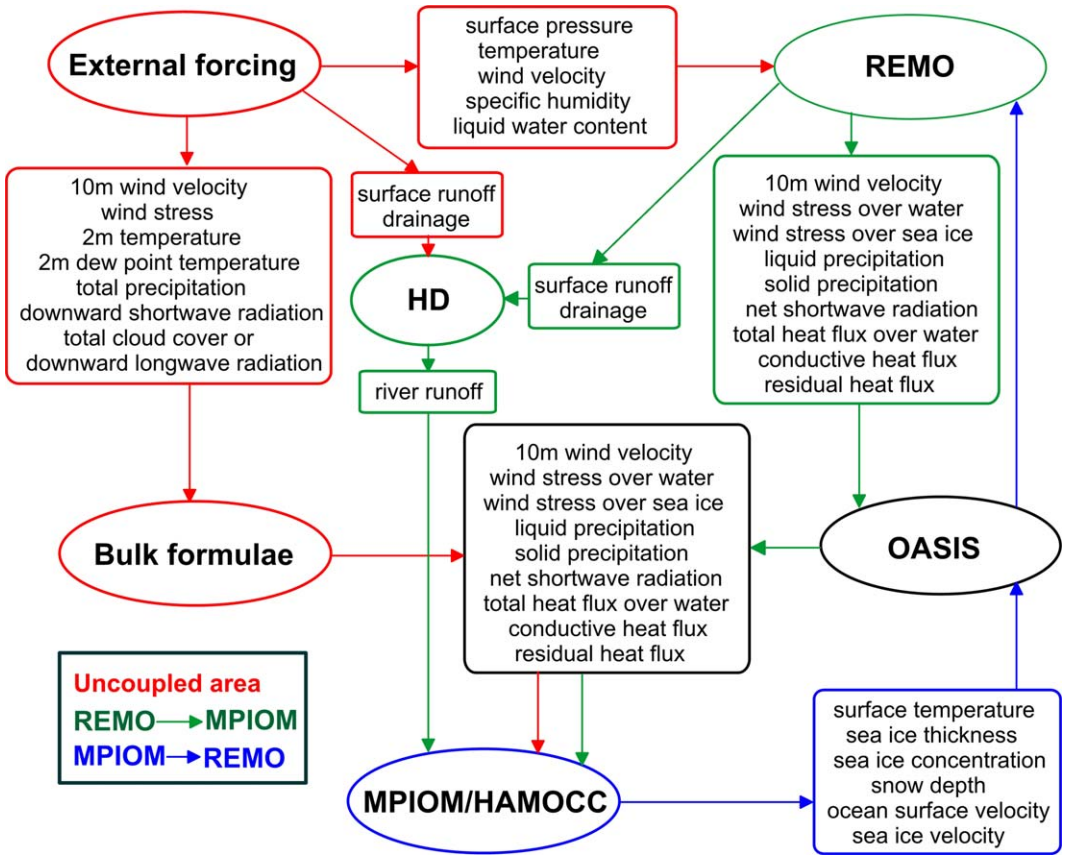

Figure 1. Coupling scheme. Red color denotes the prescribed forcing used as lateral boundary conditions for REMO and as surface forcing for MPIOM in the uncoupled area. The workflow of heat, momentum, and mass fluxes from the atmosphere (REMO) to the ocean (MPIOM) in the coupled area is marked with green. The data flow from MPIOM to REMO is marked with blue.

MPIOM. In regions covered with glaciers, which are prescribed in our model explicitly, the total precipitation is provided into the HD model. The freshwater inflow into the ocean is then calculated assuming an artificial river flow (instead of glacier flow). The replacement of the glacier flow by river flow is a simple assumption, but it allows us to close the freshwater balance over the glaciers.

3. Experimental Setup

In order to evaluate and validate the North Atlantic climate as simulated by ROM, we now analyze and compare the output of two ROM simulations carried out with the same setup (as described in section 2) but with different atmospheric forcing. For the first simulation (ROM-NCEP), atmospheric data from the NCEP/NCAR reanalysis [*Kistler et al.*, 2001] for the period 1948–2007 are used as boundary conditions. For the second run (ROM-ECHAM5), the boundary conditions are taken from a twentieth century simulation (1920–2000) with the ECHAM5/MPIOM AOGCM performed in the framework of the CMIP3 [*Roeckner et al.*, 2006].

3.1. REMO/HD Setup

The computational grid of the atmospheric model REMO used in this study has about 37 km horizontal resolution and 27 hybrid vertical levels. It covers all of Europe and parts of the Arctic and the North Atlantic (Figure 2). The model is run with ECHAM4/ECHAM5 physics. Initial and lateral boundary conditions are obtained from the same data set used for MPIOM forcing in uncoupled domain (see section 3.2), i.e., NCEP reanalysis [*Kistler et al.*, 2001] or ECHAM5/MPIOM IPCC C20 simulations [*Roeckner et al.*, 2006]. REMO obtains the lower boundary conditions over the sea and sea ice surfaces from MPIOM through the OASIS coupler every coupled time step. Simultaneously, it provides the atmospheric momentum, heat and water fluxes to the ocean model. The Hydrological Discharge model has a global setup and, thus also requires the surface runoff and drainage input outside the REMO domain (Figure 1, branches "External forcing-HD-MPIOM").

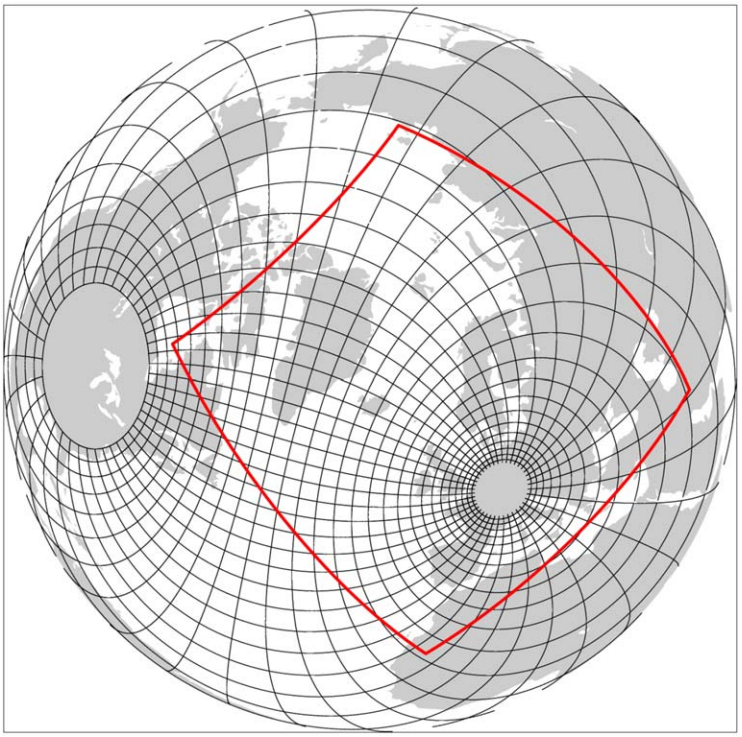

Figure 2. Grid configuration; the red rectangle contains the coupled domain, in the ocean/sea ice model grid (black lines), only every 15th line is shown.

These data were either taken from the corresponding global driving atmospheric model (ECHAM5/MPIOM in the case of scenario simulations) or generated using the MPI-M Hydrology Model (MPI-HM) [*Stacke and Hagemann*, 2012] driven by the Watch Forcing Data [*Weedon et al*., 2011] for the NCEP hindcast runs. Both the surface runoff and the drainage obtained from REMO are interpolated onto the HD grid, merged into the corresponding global data set and used as forcing in the HD model.

3.2. MPIOM Setup

The particular MPIOM setup used in this study has high resolution in the North Atlantic and in the North European shelves. The horizontal resolution gradually varies between a minimum of 5 km in the North Sea (Figure 2) and a maximum of 220 km in the Antarctic (not shown). The model has 30 vertical levels with increasing level thickness, i.e., 16, 10, 10, 10, 11, 13, 16, 19, 23, 23, 28, 33, 40, 48, 58, 70, 84, 102, 122, 148, 178, 214, 258, 311, 375, 452, 544, 656, 791, 800 m. The thickness of the first model layer (16 m) was chosen to ensure model stability. As the MPIOM does not support drying, the thickness of the upper model layer has to be larger than maximal tidal amplitude plus maximal sea ice thickness. The density ratio between sea ice and sea water was considered for this calculation.

The North Sea-Baltic Sea system was treated differently than the other oceans. The sea ice salinity in the Baltic Sea was set to 0 (instead of 5 for ocean sea ice). This was done because the minimum salinity in the Baltic Sea waters can be close to 0, and the Baltic Sea ice salinity reflects the low water salinities [*Granskog et al*., 2006]. The bottom topography of the Danish straits was corrected to provide realistic exchange between the North and the Baltic Seas. Narrow and deep trenches with a width of several hundreds of meters and a depth of up to 50 m play an important role for this exchange [*She et al*., 2007]. It is clear that we cannot resolve such trenches with a global ocean model. For this reason, the bottom topography in the straits is set as follows: (i) at least one grid box width across the strait and (ii) three active layers, i.e., the minimal depth is 36m. Three is a minimal number of layers in a *z*-coordinate model, which could simulate more or less realistic exchange flow through the shallow strait. In stand-alone mode, MPIOM is started with climatological temperature and salinity data [*Levitus et al*., 1998]. It is integrated four times through the 1948–2000

period using 6 hourly NCEP reanalysis data as forcing. Each individual run uses the end of the previous run as the initial condition.

With the ocean model running uncoupled (i.e., in stand-alone mode), an inconsistency in freshwater budget arises. While precipitation and river runoff are prescribed from reanalysis or observational data, surface evaporation is calculated by the model. To avoid the model drift caused by this inconsistency, a salinity-restoring correction is applied also to the natural freshwater fluxes. This correction is implemented by adding an additional "source" term of the form $-(S\text{-}S_{obs})/k$ to the advection-diffusion salinity equation. Hereby, S is the modeled salinity, S_{obs} is the "observed" salinity to which the computed salinity should be restored, and k is a time constant regulating the restoring speed. The details of the salinity-restoring algorithm implemented in MPIOM are described in *Marsland et al*. [2002]. In our simulations, restoring was performed for the surface layer (0–16 m) toward Polar science center Hydrographic Climatology (PHC) [*Steele et al*., 2001] with a time constant of 180 days. No salinity restoring is applied under sea ice.

The global climatology does not realistically represent the low salinities in river plumes and estuaries. To avoid unrealistically strong restoring toward too high salinities in river mouths, restoring was switched off in regions where surface salinity was less than 28 by applying a smooth transition coefficient changing from 0 ($S < 28$) to 1 ($S > 30$). To avoid an unrealistically large restoring, the absolute value of the difference $|S\text{-}S_{obs}|$ was restricted to 1.

In coupled mode, the model is started from the final state reached in the last standalone run. The initial date is 1 January 1948 for NCEP-forced runs and 1 January 1920 for ECHAM5/MPIOM-forced simulations. An earlier starting date for the ECHAM5/MPIOM-forced run was chosen because of the ocean biogeochemical spin-up (see section 3.3). Forcing time step was 6 h and coupling was done hourly.

For both the NCEP and ECHAM5/MPIOM-forced simulations, two subsequent coupled model integrations were carried out. In the uncoupled domain, inconsistencies in the freshwater budget over the ocean were leading to a substantial drift of the model. To overcome this, salinity in the surface layer (0–16 m) was also restored in the first coupled integration in the ice-free regions toward climatology in ROM-NCEP, and toward climatology plus anomalies of the ECHAM5/MPIOM model in ROM-ECHAM5. The time constant of 180 days was used as in the uncoupled simulations. In subsequent experiments, the restoring was switched off and a temporally constant freshwater flux correction was used instead. This was calculated for the period 1970–2000 from the first coupled integration. We focus on the 1970–2000 period because the years before 1969 were considered to be a transition period from the uncoupled to the coupled state. The advantage of the temporally constant freshwater flux correction is the preservation of the interannual variability. On the other hand, the restoring term corrects the sea surface salinity toward climatology, thus strongly reducing the possible drift. The necessity for additional model runs for obtaining temporally constant freshwater flux corrections is one of the disadvantages of the current approach. It should be noted that the salinity-restoring and freshwater flux correction were switched off in both the North Sea and the Baltic Sea.

3.3. HAMOCC Setup

The ocean biogeochemistry requires much longer spin-up than ocean dynamics. This fact makes it almost impossible to spin-up the biogeochemical part of the model on the highly resolved computational grid. Therefore, we ran MPIOM/HAMOCC for several thousand ($>$4000) years using a 2 times coarser grid and preindustrial forcing obtained from ECHAM5/MPIOM IPCC simulations [*Gröger et al*., 2013].

The spin-up run was carried out without tides. These permits running the model with a longer time step. The prescribed atmospheric pCO_2 was set to 278 ppm (corresponding to the year 1765). The target for this run was to obtain air-sea CO_2 fluxes varying around zero. The last 100 years of this run were integrated with enabled tides. Further 95 years were run with gradually increasing the atmospheric pCO_2 to 288 ppm (corresponding to year 1860). Subsequently, this run was integrated until 2100 with atmospheric pCO_2 following the A1B scenario (Figure 3, black curve). Additionally, another run was initialized without climate warming but forced with the CMIP3 preindustrial forcing fields and with constant pCO_2. This run was carried out to ensure that the model has no substantial model drift. Unfortunately, this run was initialized accidentally with an atmospheric pCO_2 of 278 ppm instead of 288 ppm, so that the carbon cycle cannot be assessed. However, nutrient budgets are not strongly affected by the accidental perturbation in atmospheric pCO_2 and can thus be examined for potential model drifts.

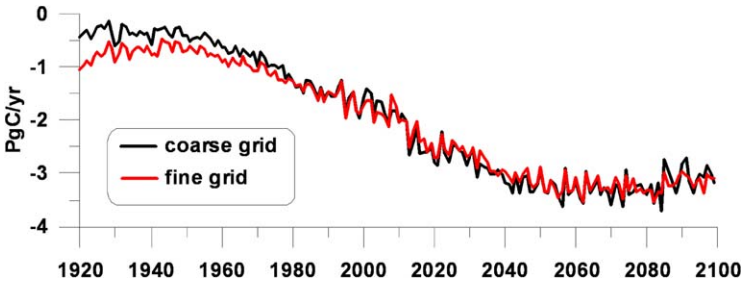

Figure 3. Annual mean globally integrated sea to air carbon flux for coarse grid (black curve) and fine grid (red line). For more details see text.

Figure 4 shows concentrations for dissolved nitrate averaged over a large part of the North Atlantic. The North Atlantic shows a trend toward slightly lower nutrient concentrations. These trends can be seen across all depth levels, which indicate that it is not a simple vertical nutrient redistribution in the water column but rather redistribution within the world ocean. However, the loss is only about 2% over the 240 years of integration. Thus, the model can be considered to be in approximate equilibrium.

After the preindustrial period, the coarser MPIOM/HAMOCC was run up to year 1920. The HAMOCC state obtained for 1 January 1920 was then interpolated to the finer oceanic grid. Starting from this date, the model simulations were carried out on the fine (original) configuration. In the shallow North Sea, all biogeochemical tracers adapt very rapidly to the finer resolution so that spin-up effects are only identified for the first few years after 1920. However, spin-up effects must be expected to act for longer in the carbon cycle. Figure 3 illustrates the time evolution of the total ocean carbon uptake in the two model setups. The coarse and the fine model configurations show similar results from 1970 onward. Therefore, we here consider the first 50 years (1920–1970) as a "transition spin-up" for the ocean biogeochemistry. Table 1 shows that the rates of carbon uptake are well within the range of other published values [e.g., *Orr et al*., 2001; *Le Querer et al*., 2009; *Ilyina et al*., 2013]. Because NCEP-forced simulations were started from 1 January 1948, they used HAMOCC initial conditions obtained from ECHAM5/MPIOM-forced run for the corresponding date.

4. Comparison With Observational Data

In this section, we present a selection of key fields from the period 1980–1999 and compare them to gridded data from different sources. These data sets are derived from observations or reanalysis data sets where appropriate. The period 1980–1999 was chosen for model validation because HAMOCC is still experiencing some adjustment before the 1980s (cf. section 3.3).

4.1. Atmosphere

In this subsection, the atmospheric component of the North Atlantic climate as simulated by ROM is evaluated. Among the pertinent variables, the mean sea level pressure (MSLP) is a good indicator for a realistic simulation of the large-scale circulation which influences near-surface temperature (T2M) and precipitation

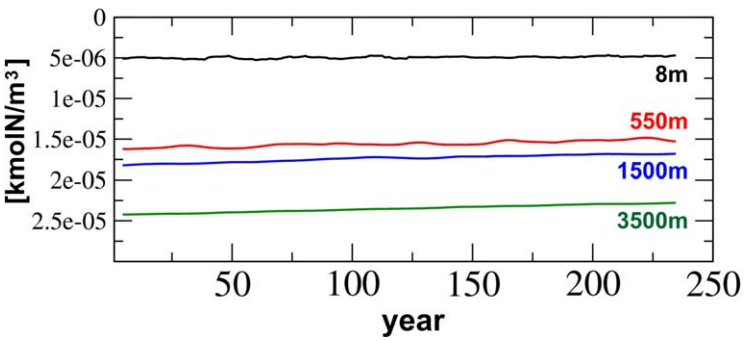

Figure 4. Mean North Atlantic (30°W–10°E; 30°N–65°N) trends in dissolved nitrate diagnosed from the coarse resolution run at different depths. Black: ocean surface, red: 550 m, blue: 1500 m, and green: 3500 m.

Table 1. Globally Integrated Carbon Fluxes in PgC/yr Averaged Over the Period 1990–1999[a]

	Other Models	This Study
Primary production	24–49[b]	49
Export production	5.0–7.99[b]	6.5
Carbon uptake ocean	1.5–2.2[c]	1.6

[a]The values are derived from an ECHAM-forced simulation.
[b]*Steinacher et al.* [2010].
[c]*Orr et al.* [2001].

distributions. Erroneous MSLP gradients induce an erroneous regional wind circulation [e.g., *Hueging et al.*, 2013], and can also have a strong effect on ocean circulation. Figure 5 displays results for MSLP for the boreal winter, defined as December, January, and February (DJF) and summer, defined as June, July, and August (JJA). The values from ERA-Interim reanalysis [*Dee et al.*, 2011] (Figures 5a and 5e) are used for comparison. ROM-NCEP provides the best agreement when compared to ERA-Interim. This is to be expected since REMO is driven by NCEP reanalysis data at the lateral boundaries, as opposed to ECHAM5 GCM data which are not constrained by observations. Deviations from ERA-Interim MSLP (Figures 5b and 5f) are within 2 hPa over most of the domain for both seasons. The largest departures are found for DJF, when negative biases occur over an area reaching from the North Sea to the Caspian Sea (up to 3 hPa). These small MSLP differences can be partially attributed to differences between NCEP and ERA-Interim reanalyses, and to biases occurring within the REMO model domain due to the model formulation. They imply comparatively small differences in terms of regional wind circulation. In summer, the ROM-NCEP MSLP is closer to ERA-Interim, with the largest positive departures located over Scandinavia. The anomalies over Greenland can be attributed to extrapolation effects below high orography.

The biases are much stronger for the ROM-ECHAM5 simulation, especially for DJF. A high-pressure anomaly is identified at higher latitudes, extending from Greenland to the Kara Sea, while a low-pressure anomaly extends from the British Isles to the Black Sea. These MSLP biases come primarily from the ECHAM5/MPIOM simulation (Figures 5d and 5f) and their magnitudes are modified by REMO: for example, the positive MSLP anomaly over the Kara Sea in DJF is moderated in REMO-ECHAM5, while the negative anomaly over the British Isles and Central Europe is exacerbated in REMO-ECHAM5 (Figures 5c and 5d). While the anomalies for JJA are weaker, the negative MSLP anomaly over northern Scandinavia is also enhanced by REMO (up to

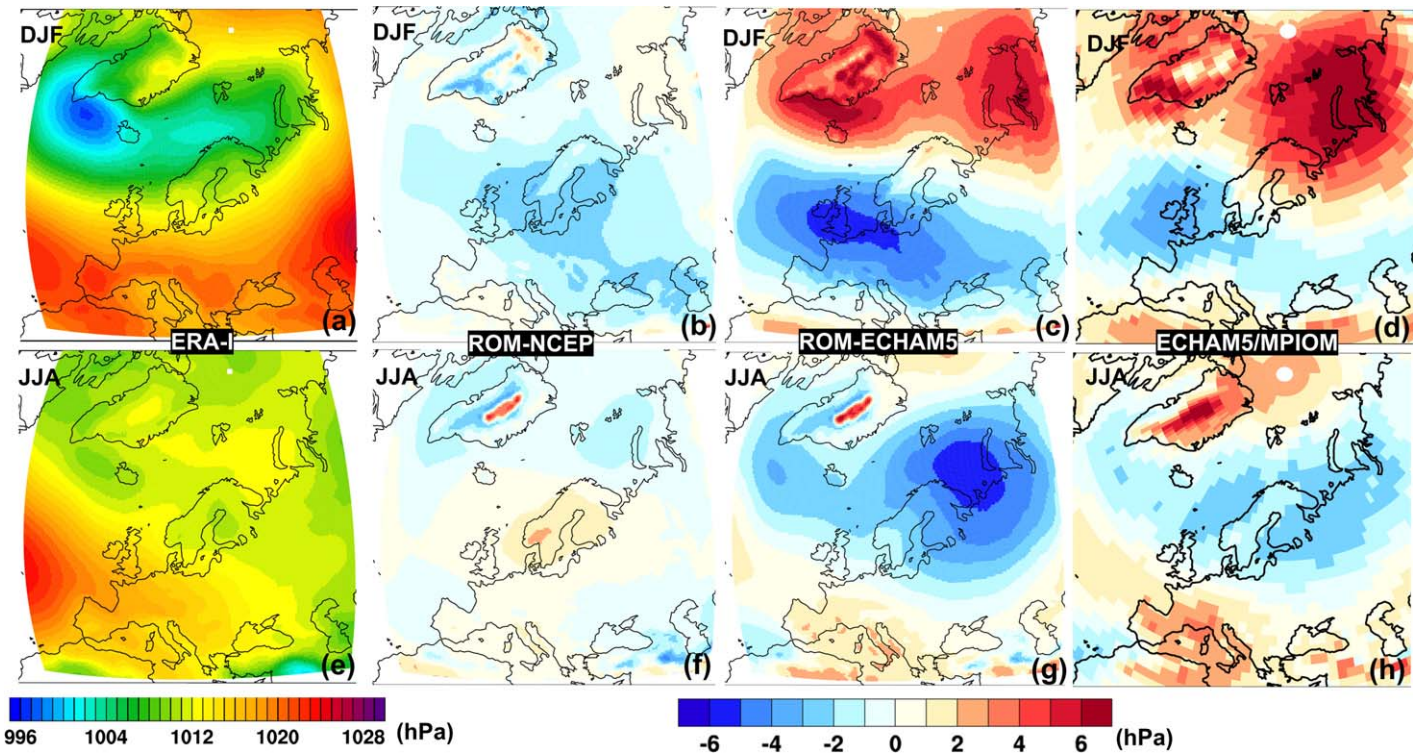

Figure 5. Mean winter and summer sea level pressure (1980–1999). (a and e) ERA-Interim and the differences Model minus ERA-Interim: (b and f) ROM-NCEP, (c and g) ROM-ECHAM5, and (d and h) ECHAM5/MPIOM.

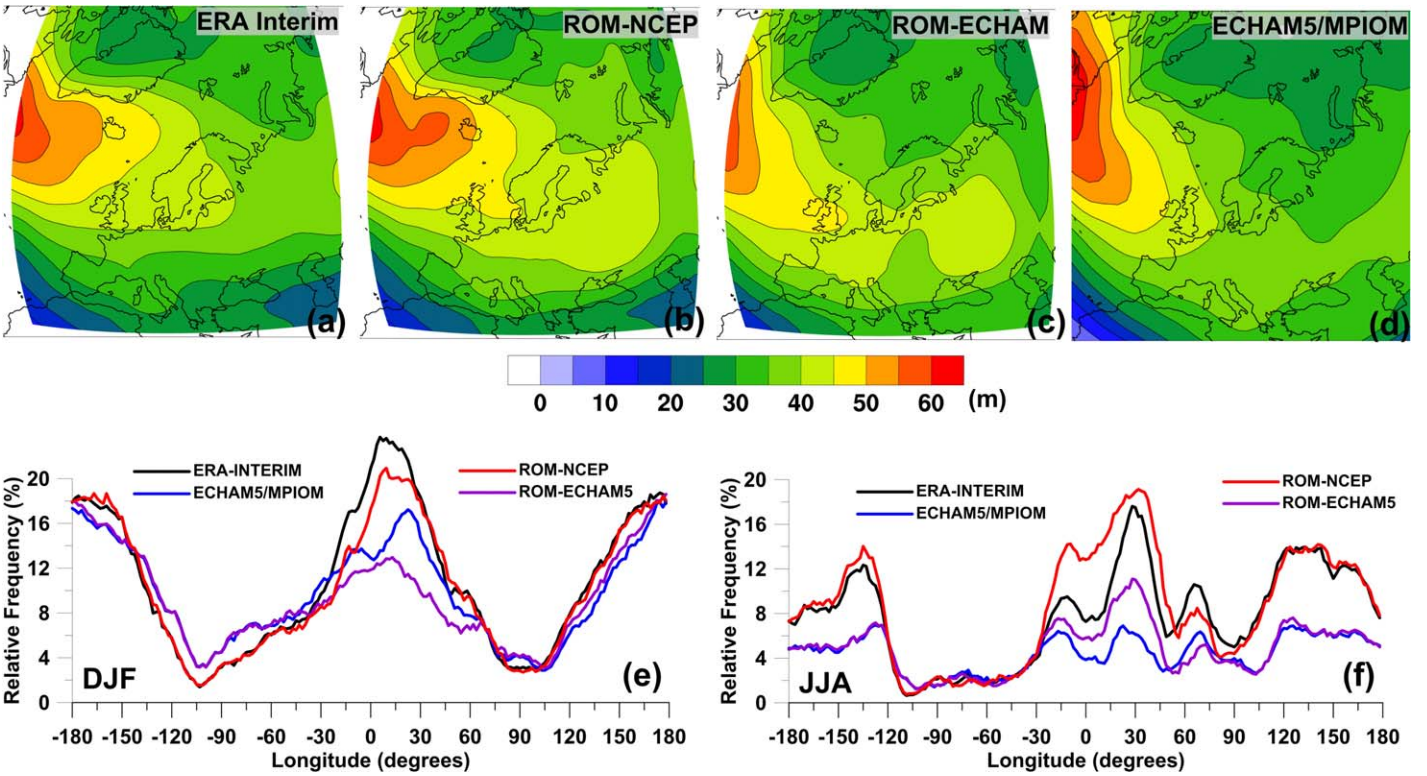

Figure 6. Standard deviation of DJF (1980–1999) band-pass filtered (2.5–7 days) 500 hPa geopotential. (a) ERA-Interim, (b) ROM-NCEP, (c) ROM-ECHAM, and (d) ECHAM5/MPIOM. (e) Winter and (f) Summer relative blocking frequency [after *Tibaldi and Molteni*,1990] calculated on daily basis. To calculate the blocking index, geopotential simulated by ROM was merged into global geopotential field obtained from corresponding driving model, i.e., ROM-NCEP was merged into NCEP and ROM-ECHAM into ECHAM5.

6 hPa, cp. Figures 5g and 5h). The changes of MLSP imply a reduction of the meridional MSLP gradient in DJF, and an enhanced north-south pressure gradient over continental Europe in JJA, thus leading to considerable changes in the near-surface winds.

The identified MSLP biases are an indication of deficiencies in the representation of the large-scale atmospheric circulation. In order to analyze this in more detail, we now consider winter storm track variability and blocking frequencies for both summer and winter. The storm track variability is quantified as the standard deviation of 500 hPa geopotential for a time window from 2 to 8 days. This variable is a rough quantification of the combined intensities and frequencies of low-pressure and high-pressure systems and thus of synoptic activity [e.g., *Hoskins and Valdes*, 1990]. As in this frequency window, the variability is dominated by low-pressure centers, the storm track intensity is primarily a measure for cyclone activity. The blocking frequencies are computed from 500 hPa geopotential height fields for reference latitude of 60°N following the approach of *Tibaldi and Molteni* [1990]. For areas where the ROM data are not available, the corresponding information from NCEP or ECHAM5 is used for the computations. Therefore, the ECHAM5/MPIOM and ROM-ECHAM5 statistics are very similar except for the longitudes correspondent to the coupled model domain. Given the excellent agreement of 500 hPa geopotential fields for NCEP and ERA-Interim (not shown), the same is true for ERA-Interim and ROM-NCEP (cf. Figure 5).

The ROM-NCEP storm track has a spatial structure and amplitude that closely resembles that of ERA-Interim (Figures 6a and 6b), although small differences are noted: for example, the area of high variability extends further into the North Sea, Scandinavia, and Eastern Europe in ROM-NCEP. On the other hand, the storm track variability for ROM-ECHAM5 is generally weaker than in ERA-interim (Figure 6c). Over Europe, the storm track is displaced to the south, which is consistent with the southward displaced MSLP gradient. These biases can also be found in ECHAM5/MPIOM (Figure 6d) [also *Pinto et al*., 2007, Figure 1].

Figure 6e shows the DJF blocking frequencies for the different data sets as a function of longitude. The blocking frequencies for ROM-NCEP (red curve) are somewhat reduced over the study area (60°W–60°E) compared to ERA-Interim (black curve). Both the ROM-ECHAM5 (purple curve) and ECHAM5/MPIOM (blue

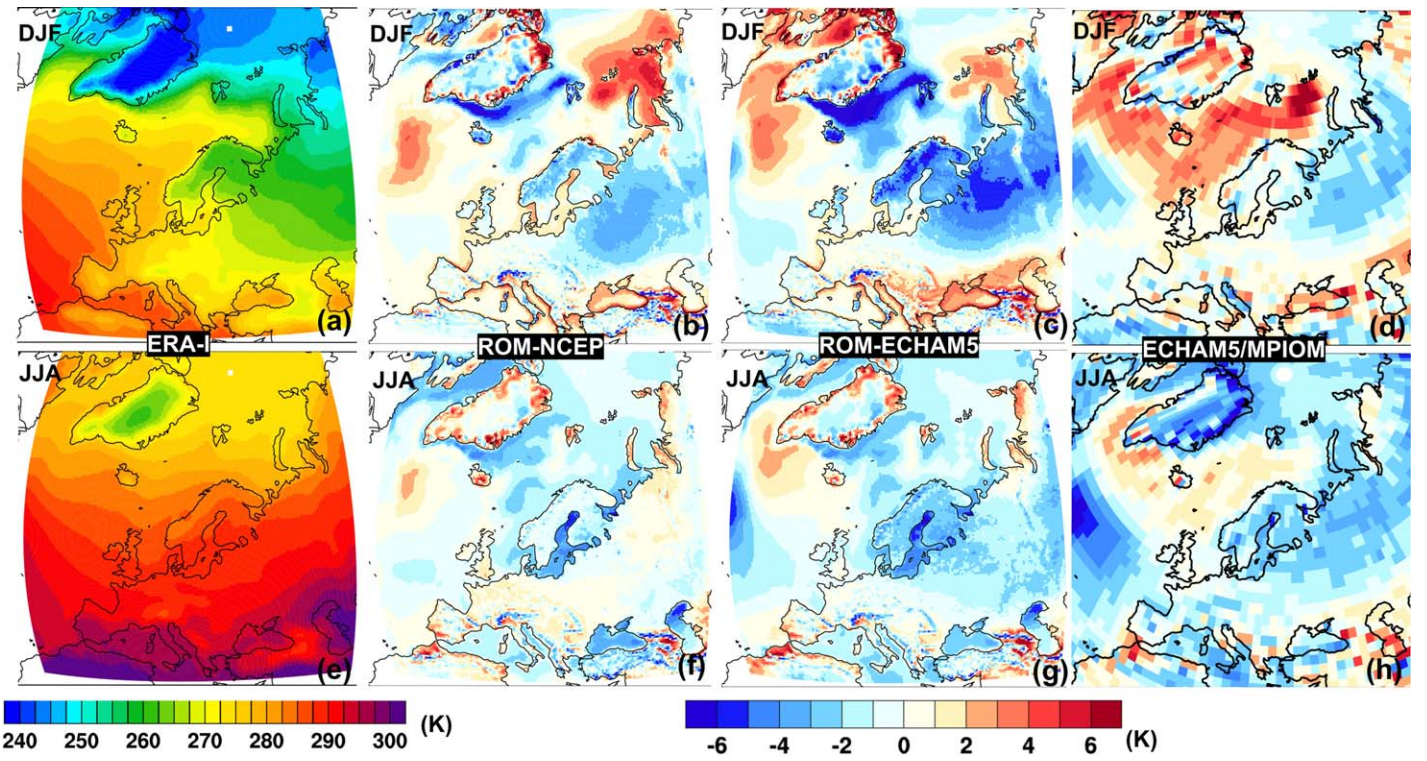

Figure 7. Mean (top) winter and (bottom) summer 2 m temperature (1980–1999). (a and e) ERA-Interim and the differences Model minus ERA-Interim: (b and f) ROM-NCEP, (c and g) ROM-ECHAM5, and (d and h) ECHAM5/MPIOM.

curve) show much lower blocking frequencies for this area, and it is clear that blocking biases are exacerbated in ROM-ECHAM5. This is in line with the above described MSLP anomalies. For the summer, the result is somewhat different: ROM-NCEP overestimates the frequency of blocking compared to ERA-Interim for the study area (60°W–60°E), while ROM-ECHAM5 actually compensates a part of the strong negative bias in ECHAM5/MPIOM. In both cases, these results are in line with the above described MSLP and winter storm track changes, and document the interesting effect that the regional model may reduce or enhance the biases of the GCM depending on the season.

The results described above have implications for regional climate, in particular for the near-surface (2 m) temperature (T2M). Figure 7 shows the differences between ROM and ERA-Interim for DJF and JJA. For ROM-NCEP, the winter departures are typically below 3 K over most of the coupled domain, except for the Barents and Kara Sea area, as well as east of Greenland (Figure 7b), consistent with corresponding sea ice thickness biases (see section 4.3 and Figure 19b). Over Europe, the departures are generally within 2 K, except for the Alpine region and an area between the Caspian and the Black Sea. Those differences can be partially attributed to differences in topography resolution.

The ROM-NCEP summer departures from ERA-Interim are generally below 2 K all over Europe and over most of the North Atlantic (Figure 7f), but shows higher discrepancies over mountainous areas. The comparatively large biases between the Black and the Caspian Sea during summer could be related to deficiencies in the soil model as well as differences in the topography. The Baltic Sea also shows a negative bias.

ROM-ECHAM5 shows a distribution of T2M biases that resembles that of the ROM-NCEP simulation, but partly with stronger, partly with weaker anomalies. ROM-ECHAM5 shows much stronger negative anomalies in winter compared to both ROM-NCEP and ECHAM5/MPIOM, which extend from Scandinavia into Russia (Figure 7c compared to Figures 7b and 7d). The T2M east of Greenland, from Iceland to Svalbard, and over the Barents Sea is strongly reduced, reversing the ECHAM5/MPIOM warm bias and increasing the ROM-NCEP cold bias east of Greenland. The SST anomalies over the North Atlantic have a strong influence on the large-scale atmospheric circulation, as the storm track location tends to be colocated with the areas of stronger meridional SST temperature gradients due to the local maximum of low-level baroclinicity. The

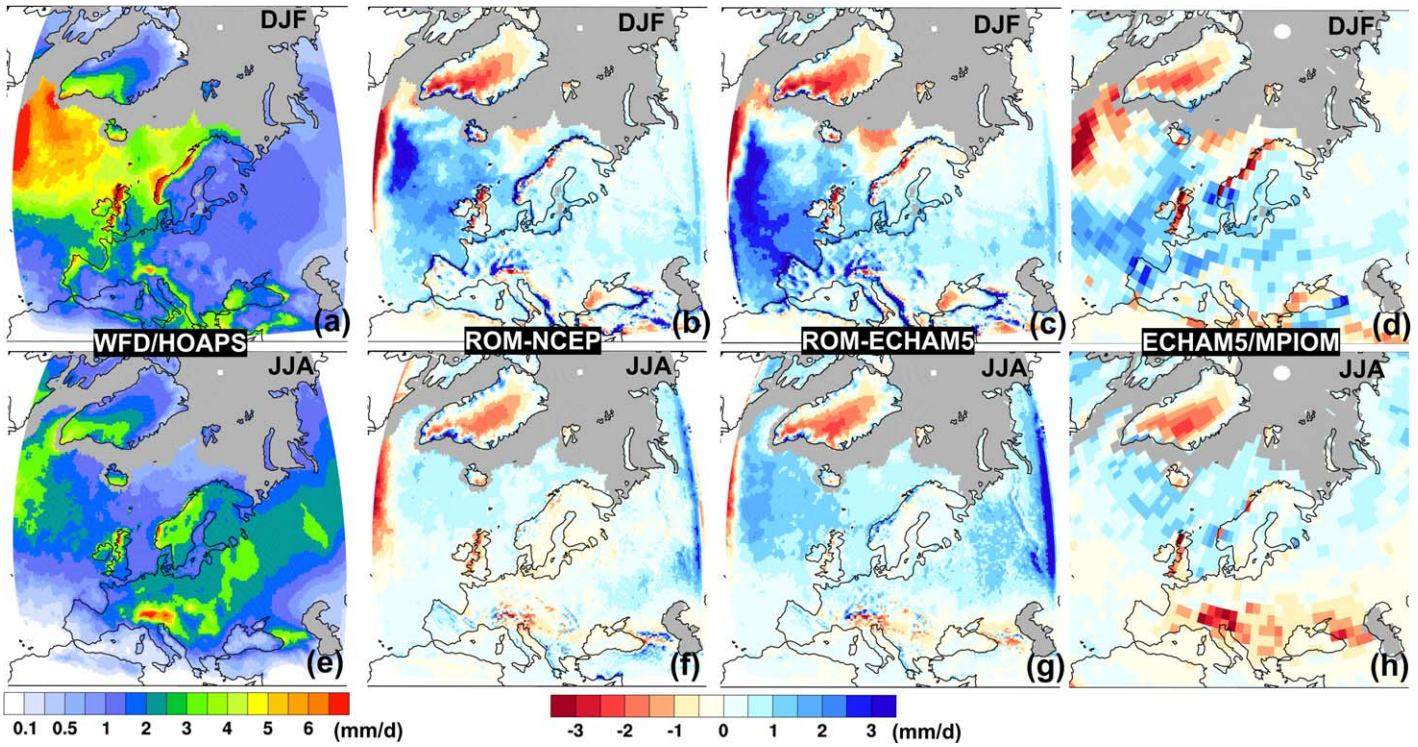

Figure 8. (a and e) Mean WFD/HOAPS winter and summer (1980–1999) total precipitation and the differences Model minus WFD/HOAPS: (b and f) ROM-NCEP, (c and g) ROM-ECHAM5, and (d and h) ECHAM5/MPIOM. Missing HOAPS data are colored with gray. Note that in contrast to Figures 5 and 7, positive biases are indicated in blue and negative in red.

different blocking frequencies (Figure 6e) and the more extensive sea-ice cover east of Greenland (section 4.3 and Figure 19) could also be partially associated with these differences. In summer, the deviations of ROM-ECHAM5 have a similar pattern to ROM-NCEP but the temperature is typically lower, increasing the ROM-NCEP cold biases (Figures 7f and 7g). This could be explained by the stronger north-south pressure gradient (Figures 5f and 5g) and the associated anomalous westerly flow and stronger maritime influence, and the reduced blocking frequencies over Eastern Europe (Figure 6f), as blocking situations in summer are associated with enhanced T2M values. Compared to ECHAM5/MPIOM (Figure 7h), the reversal of the slight warm bias over the north-eastern North Atlantic is noteworthy. This could be due to changed ocean circulation connected with higher ocean model resolution (see section 4.3). Furthermore, the cold bias over Eastern Europe is reduced in ROM-ECHAM5 compared to ECHAM5/MPIOM.

4.2. Precipitation and River Runoff

The simulated total precipitation (Figure 8) is generally overestimated in both ROM simulations over large parts of Europe, particularly for ROM-ECHAM5. This overestimation is partially due to an overestimation of the hydrological cycle in REMO, although small areas with pronounced topography such as Scotland, the mountain range in the west of Norway and some parts of the Alps stand out with negative biases. The strong biases close to the REMO lateral boundary relaxation area are a computational artifact. Within the model domain, the biases should be partially related to temperature biases (Figures 7c and 7d), as the amount of precipitable water in the atmosphere is primarily a function of temperature. The enhanced precipitation in ROM-ECHAM5 compared to both ROM-NCEP and ECHAM5/MPIOM in winter over Western Europe (Figures 8b–8d) is also associated with the southward displacement (compared to ROM-NCEP) or strengthening (compared to ECHAM5/MPIOM) of the storm track (Figures 6b–6d), thus bringing moist maritime air masses primarily toward this region. In summer, the ROM-ECHAM5 simulation shows more precipitation (Figure 8g) compared to ROM-NCEP (Figure 8f) south of Greenland, which should be primarily related to the temperature bias in ECHAM5 in the same area (Figures 7g and 7h). The increase of precipitation and decrease of temperature over Continental Europe should be related with the too strong north-south pressure gradient and the associated stronger maritime influence in ROM-ECHAM5 (Figures 5g and 5h).

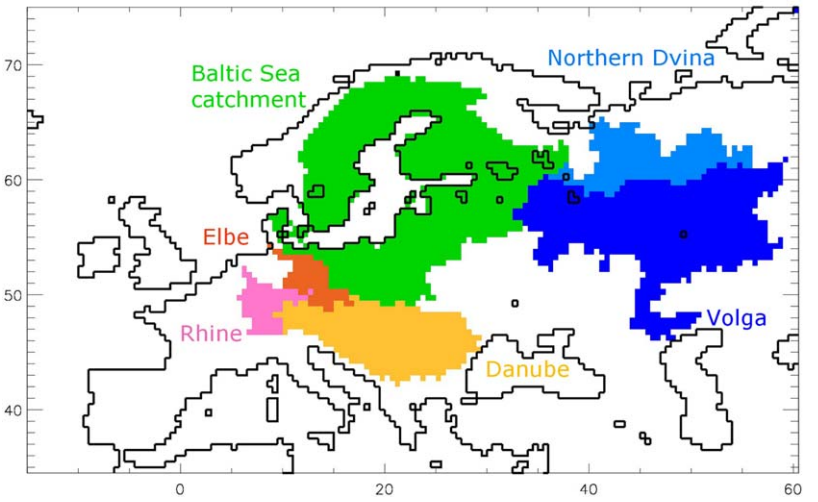

Figure 9. Large European catchments at 0.5° resolution used by HD model.

In order to evaluate the seasonal behavior of ROM and the added value of the downscaled precipitation, we consider spatial averages over several large catchments located within the regional domain (Figure 9). For precipitation observations over land, we use the WATCH forcing data (WFD) [*Weedon et al*., 2011]. Its monthly mean observed characteristics are taken from the Global Precipitation Climatology Centre full data set version 4 (GPCC); [*Fuchs et al*., 2007]. This data set is corrected for gauge undercatch following *Adam and Lettenmaier* [2003], i.e., the systematic underestimation of precipitation measurements that have an error of up to 10–50% [see, e.g., *Rudolf and Rubel*, 2005].

Figure 10 shows that the NCEP summer precipitation is too large over all catchments. The overestimation of summer precipitation over most parts of the Northern Hemisphere is a known feature of the NCEP reanalysis [e.g., *Hagemann and Gates*, 2001]. This overestimation is strongly reduced in the ROM-NCEP simulation. Moreover, the underestimated precipitation values for the other seasons are also reduced. This clearly indicates that the improved precipitation is an added value of ROM. For ROM-ECHAM5, the added value is spatially more variable. Over the Danube and Rhine rivers, an added value is provided as the so-called "summer drying problem" of ECHAM5/MPIOM is strongly reduced in ROM-ECHAM5. The problem is characterized by a too dry and too warm simulation of the summertime climate over central and Eastern Europe and is often reported for global and regional AGCMs [*Hagemann et al*., 2009]. Over the Baltic Sea catchment, ROM-ECHAM5 precipitation is closer to WFD data than ECHAM5/MPIOM from January to April, while it is somewhat worse in August and September. A similar behavior can be seen for the Elbe catchment. For both North Eastern European catchments (Northern Dvina and Volga), ROM-ECHAM5 largely overestimates precipitation in summer and autumn, while ECHAM5/MPIOM is comparatively close to the WFD data, so that the downscaling provides no added value in this case.

The discharge simulated by the HD model captures the observed seasonal cycles of discharge quite well (Figure 11). Usually deficiencies in simulated precipitation are propagated into discharge, which shows analog biases: overestimation for Baltic Sea, Northern Dvina, Volga (both ROM-NCEP and ROM-ECHAM5), Elbe, and Rhine (only ROM-ECHAM5) and underestimation for Danube (especially ROM-NCEP). For example, for the Baltic Sea, catchment precipitation is 11–14% larger than WFD data, which leads to a 23–31% overestimation of river runoff into the sea for ROM-NCEP and ROM-ECHAM5, respectively. Nevertheless, the seasonal cycle of the total river runoff into the Baltic Sea is captured well representing the maximum in May and two local minima in February and September. The snow melt-induced discharge peaks for Baltic Sea, Northern Dvina and Volga are well timed, but for the latter two catchments the decreasing flank is delayed due to the overestimated precipitation. This is particularly the case for the Volga, where the simulated maximum discharge is delayed by one month.

4.3. Ocean and Sea Ice

The comparison between mean sea level obtained by ROM and ECHAM5/MPIOM is shown in Figure 12. The finer resolved ocean model is capable of reproducing some important features that are missing in the coarser ECHAM5/MPIOM version, e.g., the better representation of the Gulf Stream separation and the

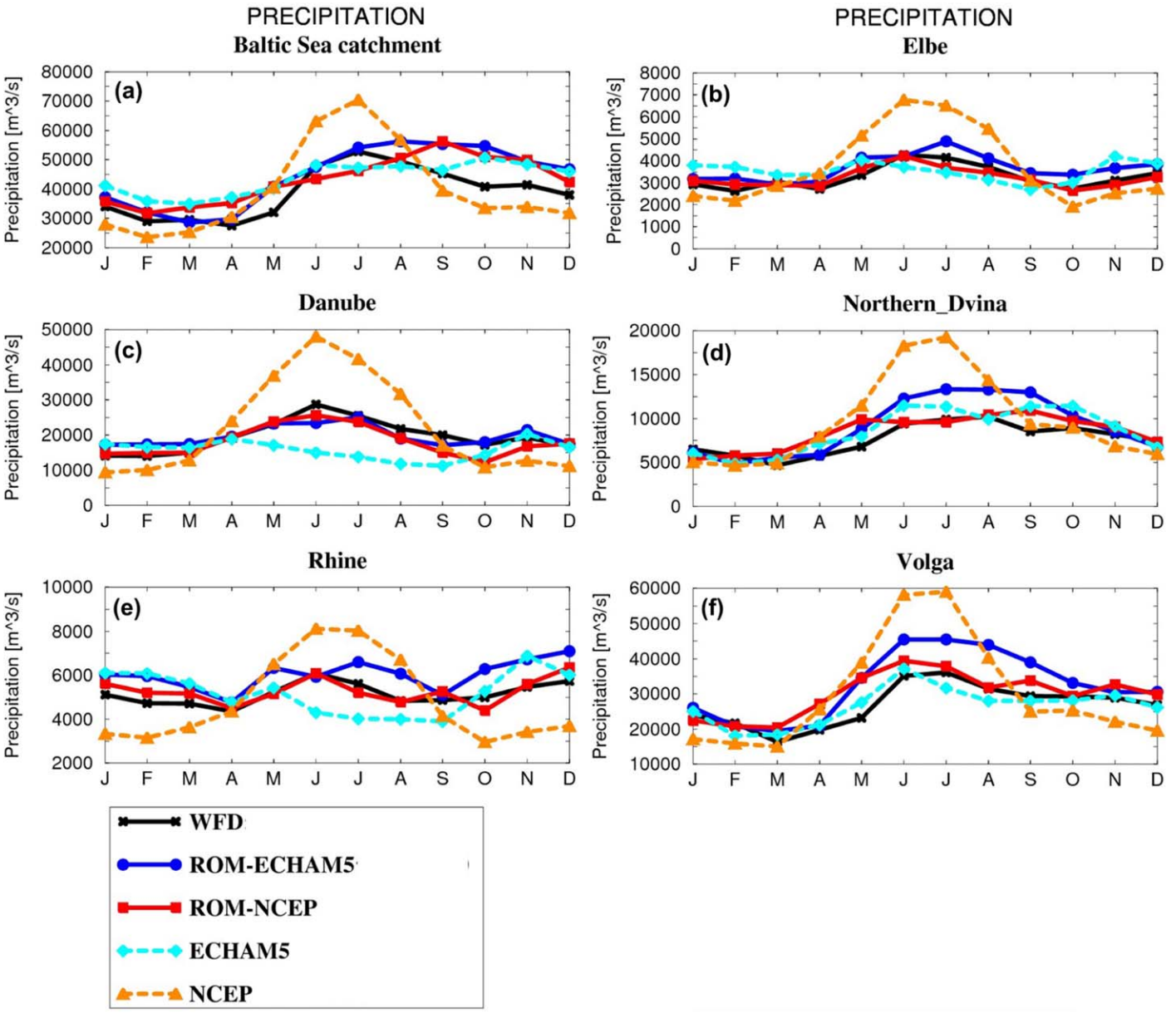

Figure 10. Catchment averaged precipitation 1980–1999 (m^3/s). (a) Baltic Sea catchment, (b) Elbe, (c) Danube, (d) Northern Dvina, (e) Rhine, and (f) Volga.

Labrador Current. In ECHAM5/MPIOM simulation (Figure 12b), there is an unrealistic south-eastward extension of Subpolar Gyre (SPG). This feature can be explained by the coarser resolution of the ocean grid, and consequent "late" separation of the Gulf Stream causing the "blocking" of the Labrador Current, which leads to the eastward spread of the Labrador Sea water. Comparing NCEP and ECHAM5/MPIOM-forced runs (Figures 12c, 12d, 13a, and 13b), an overestimation of the Labrador Current is also seen in the second case (Figures 12d and 3b). This overestimation could be due to the fact that ECHAM5-forced run provides stronger outflow from the Arctic (Figure 13b). Additionally, the ECHAM5/MPIOM atmospheric forcing leads to a larger amount of sea ice in the Arctic (see below) and enhanced freshwater cycle in the high latitudes. Both these features increase Arctic freshwater export and its consequent accumulation in the SPG. The main difference in ROM-ECHAM5 compared to ECHAM5/MPIOM is that the Labrador Sea water released from the SPG is not blocked by the "late separated" Gulf Stream, and can flow along the North American coast. Despite this improvement, an unrealistic southward extension of the SPG and consequent overestimated zonality of the North Atlantic current is found in all the simulations.

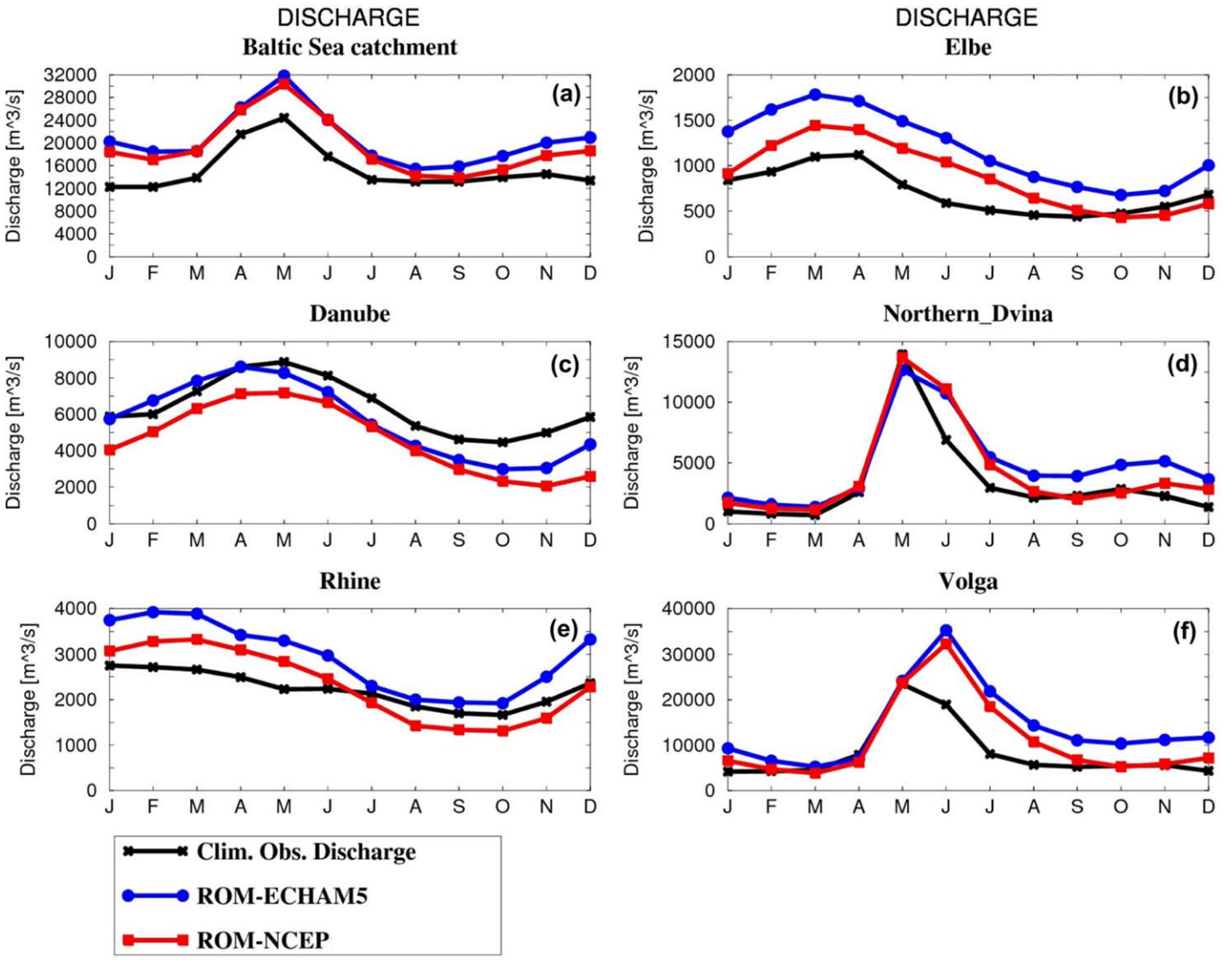

Figure 11. Observed and simulated mean annual cycle of river discharge, 1980–1999 (m^3/s). (a) Baltic Sea catchment, (b) Elbe, (c) Danube, (d) Northern Dvina, (e) Rhine, and (f) Volga.

We hypothesize the following explanation: in observations, the Labrador Sea water is sinking and flowing as upper deep water or intermediate water southward. Additionally, the Labrador Current, consisting of the fresh and cold surface water of the Labrador Sea, flows southward along the coast. In this case, a stronger North Atlantic current tends to reduce the Labrador Current coming from the opposite direction. In our simulations, the southward Labrador outflow in ROM-ECHAM5 is stronger than in ROM-NCEP due to more intense SPG, thus tending to "force" the North Atlantic current southward and Gulf Stream eastward. As different atmospheric data were used to force the same ocean model, we conclude that the overestimated eastward shift of the Gulf Stream as well as the excessive zonality of the North Atlantic current in ROM-ECHAM5 are caused by biases in the atmospheric forcing (section 4.1).

Atlantic meridional overturning circulation (AMOC) in ROM-ECHAM5 and ROM-NCEP differs significantly both in intensity and the vertical structure (Figure 14). The maximum of AMOC simulated by ROM-ECHAM5 reaches ~20 Sv, whereas in ROM-NCEP it is about 18 Sv, which seems to be more realistic. A value of approximately 18.5 Sv has been estimated from the RAPID array [*Cunningham et al.*, 2007]. The reason for the overestimated AMOC in ROM-ECHAM5 can be due to the enhanced deep water convection in the Labrador Sea and stronger SPG. In terms of vertical structure, the Antarctic bottom water (AABW) cell in ROM-ECHAM5 is strongly reduced in comparison with ROM-NCEP results (Figure 14).

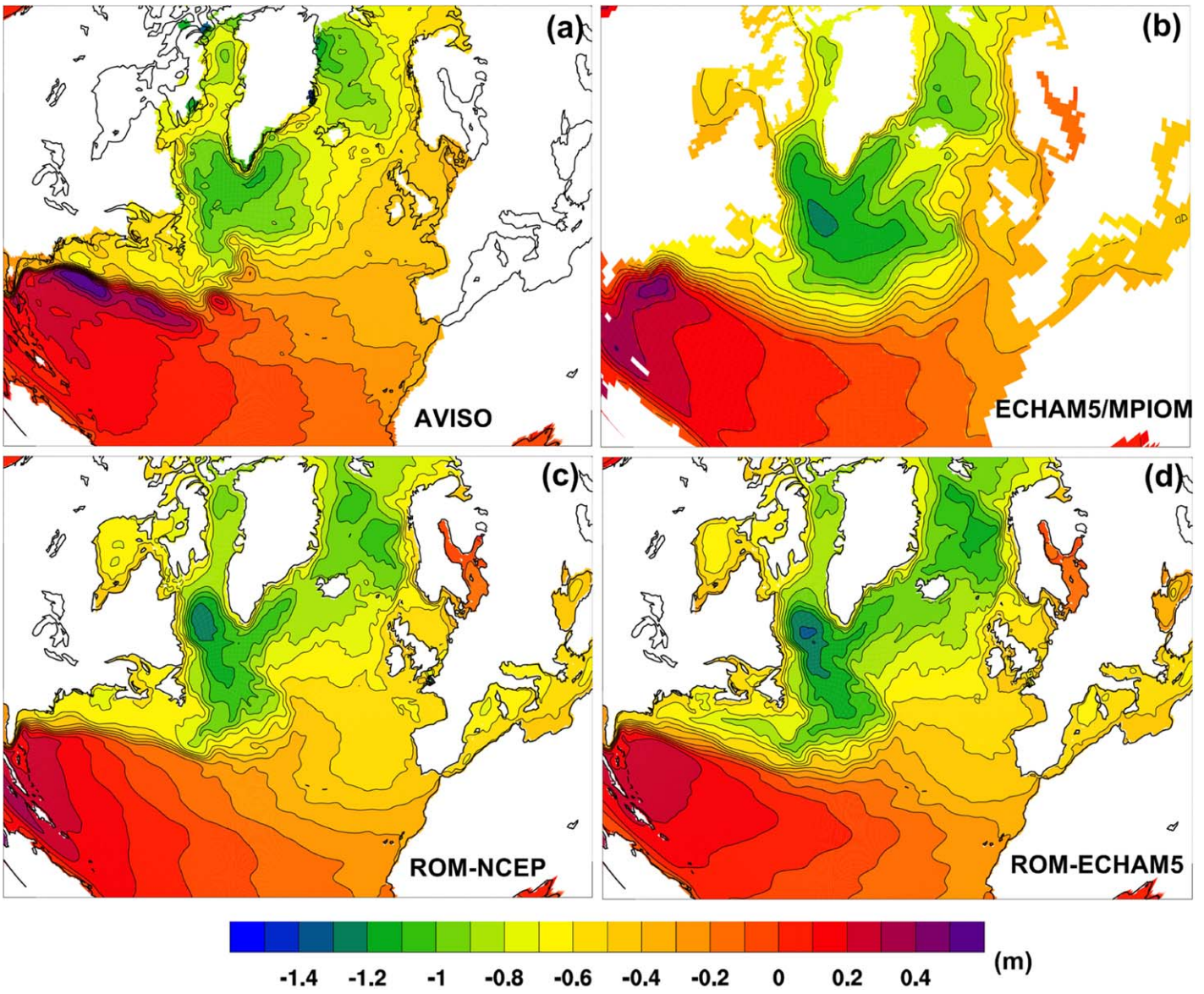

Figure 12. Mean (1980–1999) sea level. (a) AVISO data [*Schaeffer et al*., 2012], (b) ECHAM5/MPIOM, (c) ROM-NCEP, and (d) ROM-ECHAM5.

The ocean tidal forcing was derived from the full ephemeridic lunisolar tidal potential [*Thomas et al*., 2001]. For validation purposes, a least squares harmonic analysis of sea level was performed. The ability of the model to simulate tidal dynamics is shown in Figure 15. Here we present only the M_2 constituent, which is the dominant component in the domain of our interest. In the eastern part of the North Atlantic the agreement between the model and observation is reasonable for a climate model. The amphidromic points are well captured, especially in the Greenland, Iceland, Norwegian (GIN) seas and North Sea. In the western part of the North Atlantic, the disagreement between the model and observation is much larger. The tidal amplitude is strongly overestimated in the Labrador Sea, leading to the eastward shift of North Atlantic amphidromic point and underestimated along the U.S. coast. The higher tidal amplitude in the Labrador Sea could be explained by reduced tidal energy transfer through the Hudson Strait into the Hudson Bay, where the amplitude is strongly underestimated. This reduction leads to the "accumulation" of tidal energy in the Labrador Sea, which results in the increase of the amplitude.

In our region of interest, in particular at the North European shelves, ocean tidal dynamics plays an important role. Its influence on the climate was investigated by *Müller et al*. [2010]. Using the global coupled

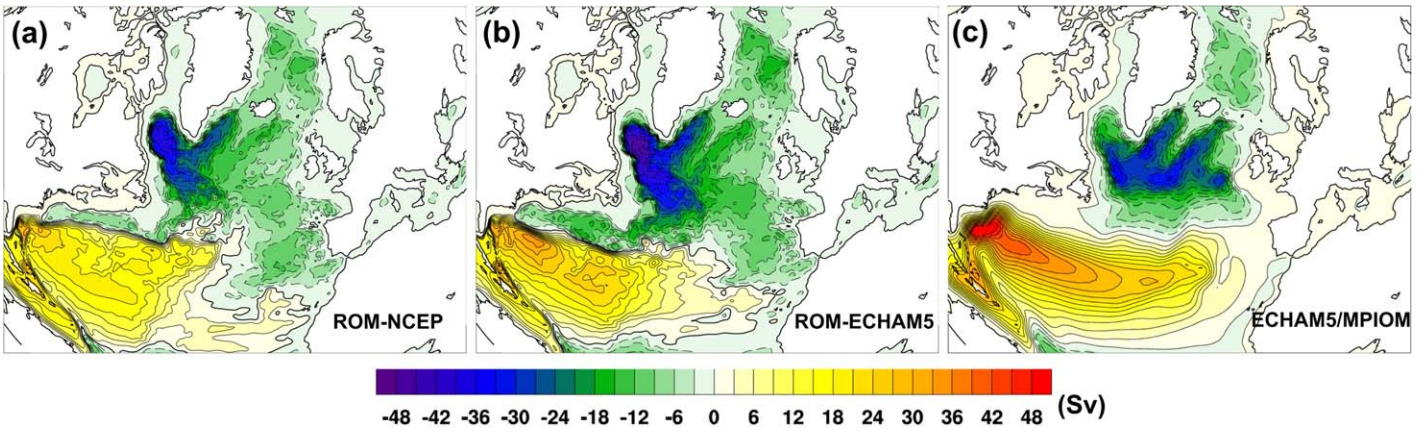

Figure 13. Mean (1980–1999) barotropic stream function. (a) ROM-NCEP, (b) ROM-ECHAM5, and (c) ECHAM5/MPIOM.

atmosphere-ocean general circulation model (AOGCM) ECHAM5/MPIOM, they showed significant changes in the North Atlantic circulation caused by the induced tidal mixing and nonlinear interactions of tides with low-frequency motion. Comparing two sets of our simulations (with and without tidal forcing) we also found some pronounced differences in the spatial structure of the circulation "ring": Gulf Stream-North Atlantic current-SPG-Labrador Current-Gulf Stream. Tidal stress interaction with irregular bottom topography generates an additional eddy field, whose energy is partly transferred to the mean field in form of a basin-scale steady cyclonic circulation. This effect is known as Neptune [*Holloway*, 1987, 1992] and induces changes in the barotropic stream function of the North Atlantic as compared to the nontidal simulations. These changes cause a further southward penetration of the Labrador Current, which "pushes" the Gulf Stream southeastward. Evidence supporting this conclusion is presented in Figures 15c and 15d, showing the concentrations in the upper 200 m of a numerical tracer whose concentration is kept constant and equal to unity south of 23°N and with a half-time decay of 30 years. The plots show the mean tracer concentration and its relative difference from nontidal run in the years 1980–1999, starting the simulations with and without tides from the same tracer concentration field in the year 1920. Figure 15c shows the concentration of the numerical tropical tracer in the tidal simulations, identifying the presence of waters of tropical origin. As expected, a steep front in tracer concentration separates the tropical Gulf Stream from the Arctic Labrador Current. Figure 15d depicts the relative difference between the tropical tracer concentration distribution with and without tides. There is a remarkable reduction in the tropical tracer concentration (10–20%) along the North American east coast down to Cape Hatteras, clearly pointing out a better

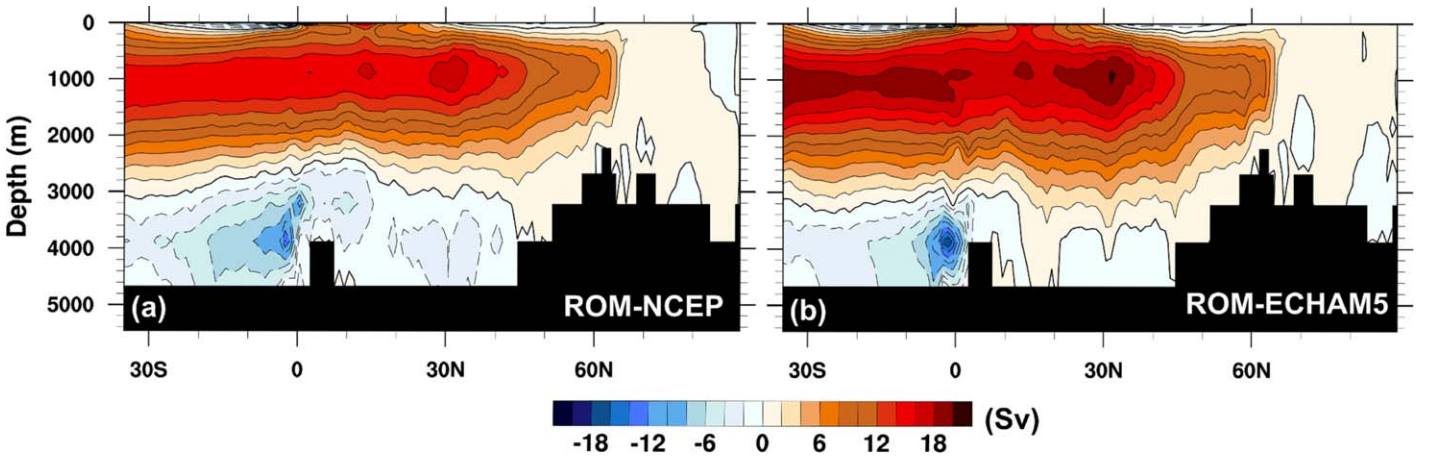

Figure 14. Mean Atlantic meridional overturning stream function averaged for 1980–1999 (Sv).

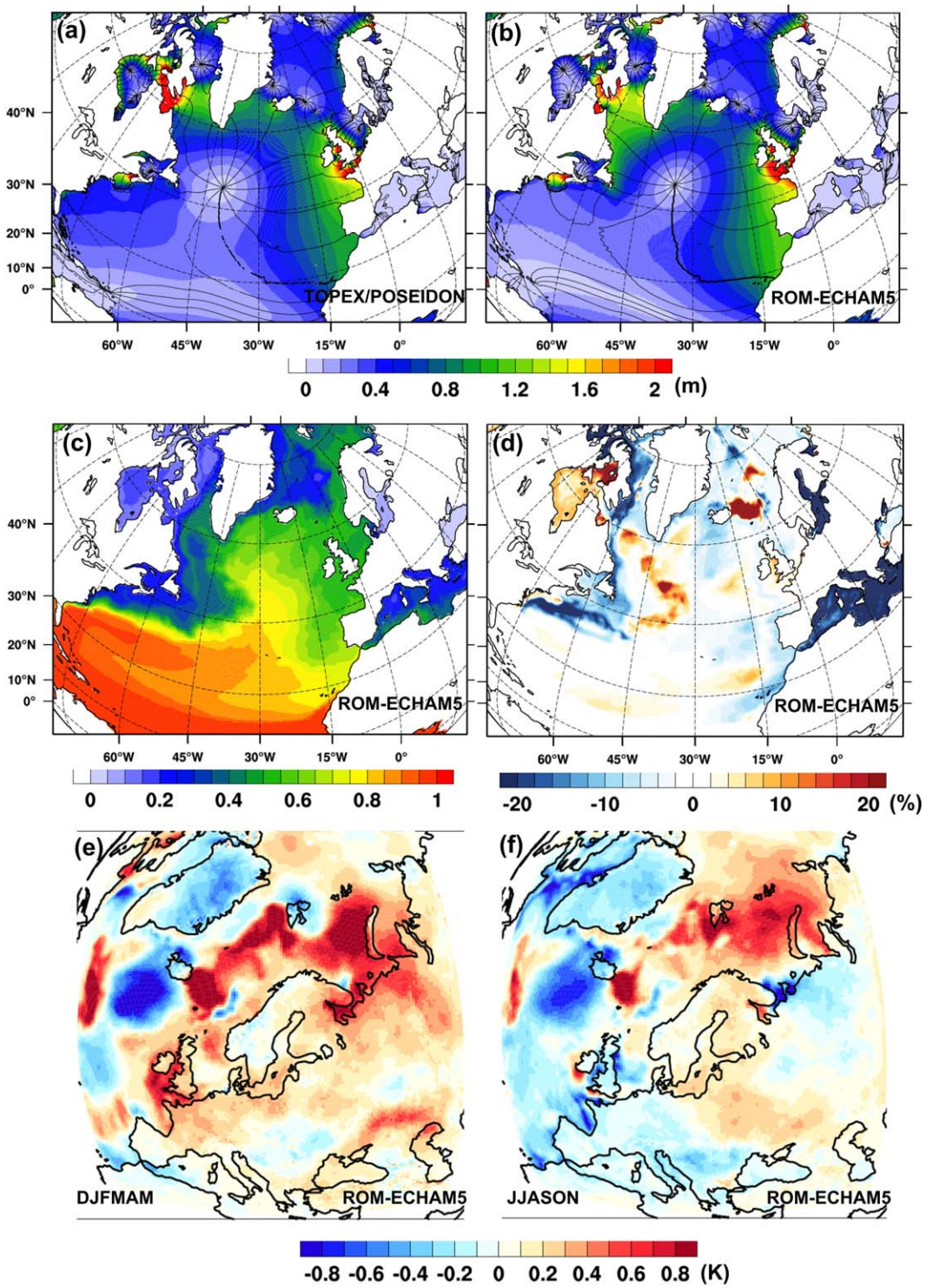

Figure 15. (a) Observed and (b) modeled M_2 tidal maps. Cotidal lines are with 30° interval. (c) Mean 0–200 m passive tropical tracer concentration in the simulation with tides and (d) its relative change (%) from the simulation without tides. (e) Winter/Spring and (f) Summer/Autumn 2 m temperature difference between the simulations with and without tidal forcing.

representation of the Gulf Stream separation because the Labrador Current waters penetrate further south due to the inclusion of tides. The consequent shift of the North Atlantic current and the tidal circulation around the North Atlantic amphidromy supply more salty Atlantic water into the SPG, thus increasing its strength and convection activity in the Labrador Sea.

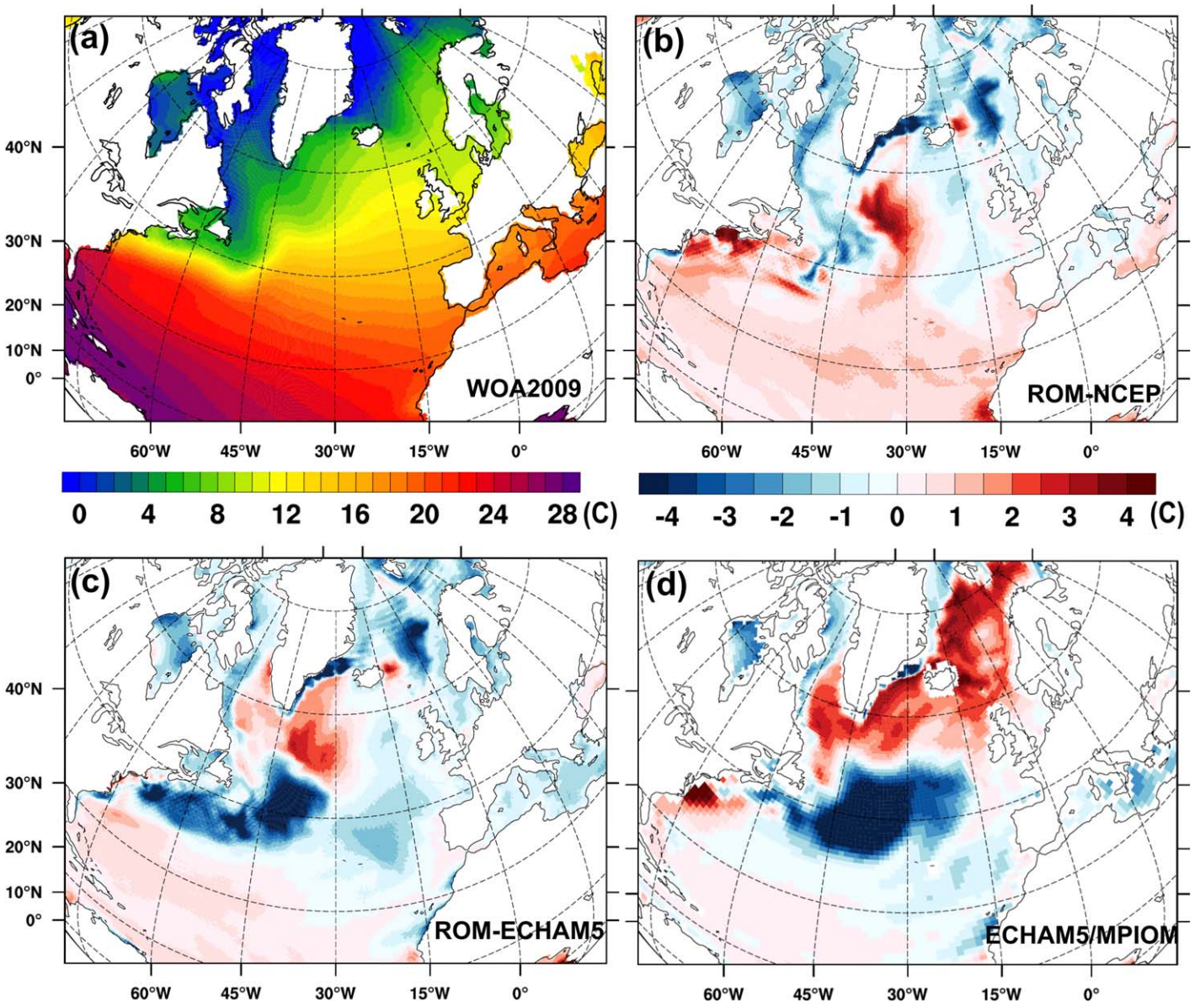

Figure 16. (a) Mean (1980–1999) sea surface temperature (SST) WOA2009 climatology and differences Model minus WOA2009: (b) ROM-NCEP, (c) ROM-ECHAM5, and (d) ECHAM5/MPIOM.

Additionally, our experiments show some tidal impact on the modeled climate over Europe (Figures15e and 15f). Its influence on the Western European temperature can be clearly explained by the increased mixing. Still, there are large spatial variations. The winter and spring mean 1980–1999 2 m temperature is 0.2–0.4 K warmer, whereas in summer and autumn it is 0.2–0.4 K colder.

The biases in ocean circulation described above are clearly reflected in the biases of SST and SSS (Figures 16 and 17). Strong cold SST bias (up to 4 K) in ROM-ECHAM5 between 40°W and 60°W can be explained by the shift of the North Atlantic current in this simulation. An absence of this bias in ROM-NCEP (Figure 16b) indicates that its origin comes from the ECHAM5/MPIOM atmospheric forcing (Figure 16d). The negative salinity bias in the ROM-ECHAM5 results (Figure 17c) shows a similar structure compared to the SST bias, indicating the overestimated southward propagation of the fresher Labrador Sea water (Figures 12d and 13b). Figures 17e and 17f show that the above mentioned negative SSS bias is not caused by the freshwater flux correction, but mainly connected with overestimated Labrador Sea water inflow in this region. First, the freshwater correction in the Labrador Sea is negligible compared to the natural freshwater input (Figures

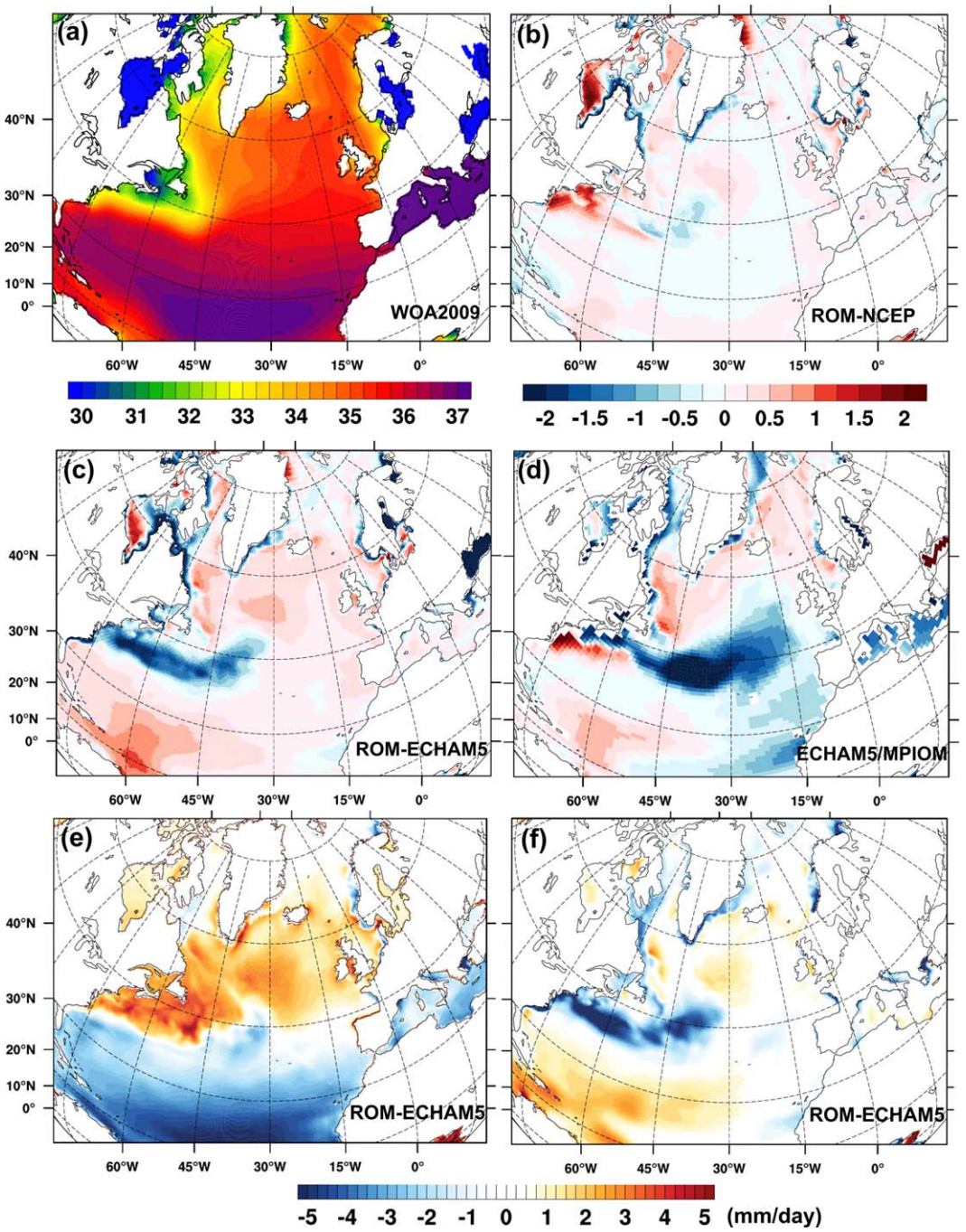

Figure 17. Mean (1980–1999) sea surface salinity (SSS) and freshwater flux from (a) WOA2009 climatology and differences Model minus WOA2009: (b) ROM-NCEP, (c) ROM-ECHAM5, and (d) ECHAM5/MPIOM. (e) ROM-ECHAM5 natural (noncorrected) freshwater flux to the ocean and (f) freshwater flux correction due to salinity restoring.

17e and 17f). Second, the location of described bias salinity-restoring tries to make the water saltier, but is too weak to eliminate the bias.

Another cold SST bias simulated by ROM forced by both ECHAM5/MPIOM and NCEP atmospheres occurs in the Norwegian Sea (Figure 16). A possible explanation is the reduced oceanic heat transport into Norwegian Sea due to the excessive zonality of the North Atlantic current. On the other hand, there is a strong difference in SST bias between ROM-ECHAM5 (strong cold-bias) and ECHAM5/MPIOM (strong warm-bias) in GIN seas. This difference can be explained by the difference in ocean models resolution. Whereas ROM-MPIOM

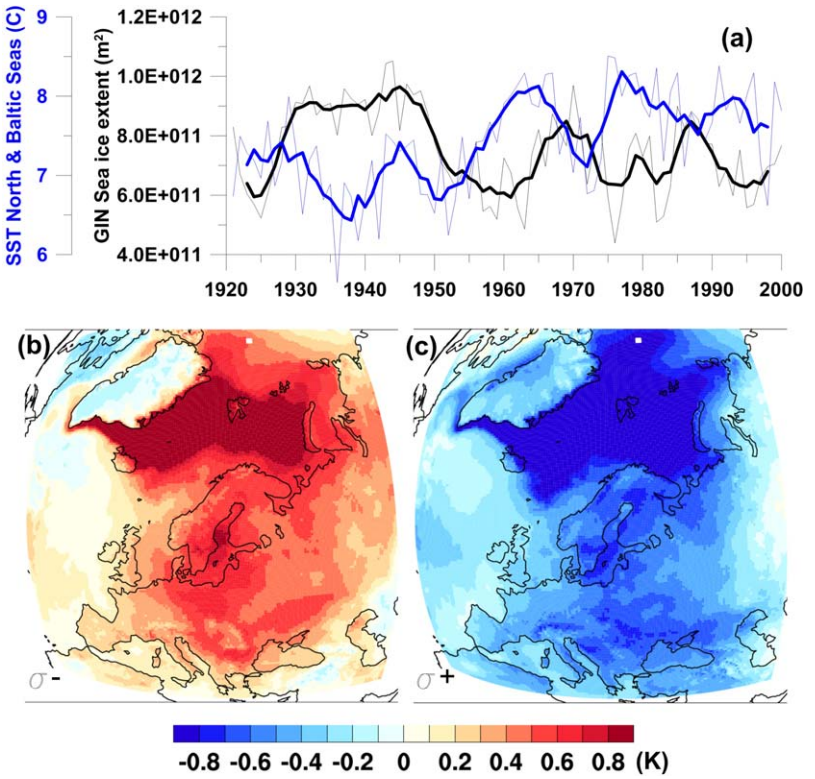

Figure 18. (a) Annual mean sea ice extent in the GIN Sea (black) and SST in North and Baltic Seas (blue). Thick lines—5 years running means. (b and c) The composites of 2 m temperature (T2M) anomalies calculated for 1920–2000. (b) Mean T2M anomalies for the years when GIN Sea ice extent is lower than its multiyear mean minus standard deviation, and (c) mean T2M anomalies for the years when GIN Sea ice extent is larger than its multiyear mean plus standard deviation.

permits mesoscale eddies development and meandering of the North Atlantic Current (NAC), the coarsely resolved ECHAM5/MPIOM does not properly represent these features, leading to the advection of almost all of the warm NAC waters into the Arctic (Figures 13b and 13c).

The cold bias in ROM-ECHAM5 is also consistent with positive GIN seas sea ice extent anomalies. In our simulation, years with anomalously high sea ice extent in the GIN seas coincide with anomalously low SST in North and Baltic seas (Figure 18a). Simultaneously, the 2 m temperature is anomalously low over the GIN seas, Barents Sea, parts of the Arctic Ocean and Northern and Central Europe (Figures 18b and 18c).

The simulated climatological sea surface temperature in the North Sea and the western part of the Baltic Sea is in a good agreement with observational climatologies (Figure 16). In the eastern part of the Baltic Sea, i.e., Gulf of Bothnia and Gulf of Finland, SST is underestimated by about 2 K for ROM-ECHAM5. This is mainly caused by a cold bias in the atmospheric model in this region (Figure 16d), which is subject of further investigations. The largest disagreement of sea surface salinity on the North European shelves with observational data occurs around Denmark, in the Gulf of Finland and at the Norwegian coast (Figure 17). Both the vertical and the horizontal resolutions of the ocean model are not sufficient for a realistic representation of the physical processes in these regions. Note that both in the North and Baltic seas the freshwater correction in our simulations was completely switched off (see section 3). The strong model bias in the Wadden Sea is a consequence of the coarse vertical resolution. The dipole structure of salinity bias along the Norwegian coast is caused by relatively "smooth" modeled Baltic water outflow. The strong observed meandering of this outflow [*Johannessen et al*., 1989] and a consequent increased horizontal mixing with North Sea water is not resolved in our MPIOM setup.

One of the most complicated tasks in the modeling of the water circulation in the Baltic and the North seas is the representation of their exchange through the Danish straits. We realize that a vertical resolution of $\sim$10 m and a horizontal resolution of $\sim$10 km are not sufficient to reproduce exactly the high-frequency dynamics, associated with the pulse-like Baltic-North Sea water exchange through the small straits.

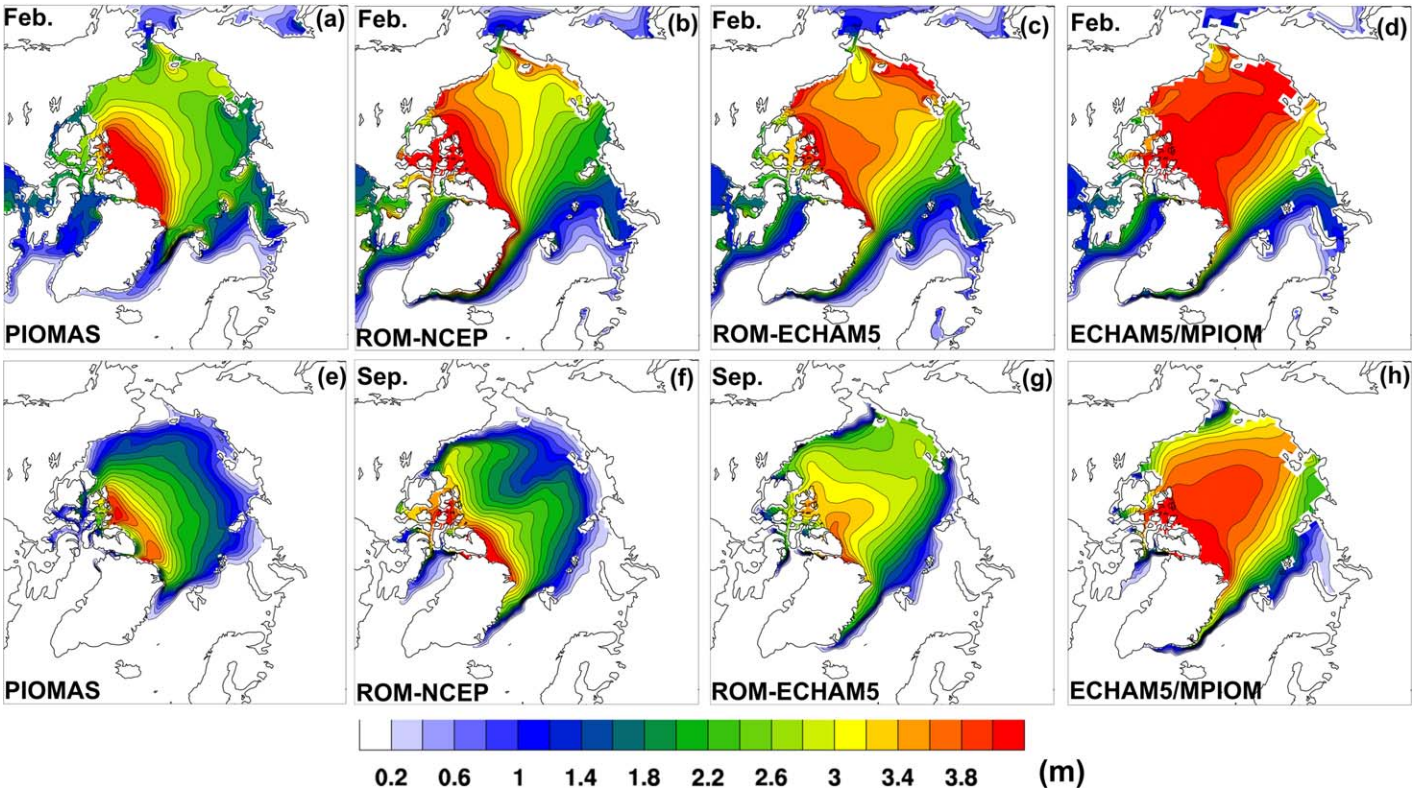

Figure 19. Mean 1980–1999 (a–d) February (e–h) and September sea ice thickness for PIOMAS (Figures 19a and 19e), ROM-NCEP (Figures 19b and 19f), ROM-ECHAM5 (Figures 19c and 19g), and ECHAM5/MPIOM (Figures 19d and 19h).

Nevertheless, the modeled salinity of the Baltic Sea is in relatively good agreement with the observational data. As we do not use any kind of freshwater flux correction or salinity restoring in this region, this indicates that the total exchange was in balance with precipitation and river runoff into the Baltic Sea.

Sea ice thickness is presented in Figure 19. The simulations are compared against the PIOMAS Arctic Sea Ice Volume Reanalysis data [*Zhang and Rothrock*, 2003; *Schweiger et al*., 2011]. The results of ROM-ECHAM5 simulations show an overestimation of the Arctic sea ice extent as well as an overestimation of the ice thickness in the Central Arctic and East Siberian Sea. The last fact can be explained by the bias of MSLP of Aleutian Low in ECHAM5 [e.g., *Roeckner et al*., 2006] and consequent reduction of atmospheric heat transport from the Pacific Ocean. The NCEP-forced simulations provide more realistic sea ice distribution in Arctic, indicating that the sea ice thickness overestimation in ROM-ECHAM5 is mainly caused by the atmospheric forcing. This fact is clearly demonstrated by the results obtained from the ECHAM5/MPIOM simulations (Figures 19d and 19h) where the ice thickness is overestimated by a factor of two in many parts of the Russian Arctic.

4.4. Ocean Biogeochemistry

We now compare the simulated distributions of dissolved nutrients, i.e., PO_4^{3-} and NO_3^- to observations from the World Ocean Atlas (WOA) [*Garcia et al*., 2009]. The model reproduces the low concentrations within the oligotrophic subtropical gyre and the higher concentrations in the Atlantic north of 40°N (Figure 20). The latter result from reduced biological consumption during winter, when phytoplankton growth is limited by solar radiation and from upward mixing of nutrients during deep winter mixing. The locally enhanced phosphate concentration near the coast of NW Africa is also reproduced. The NCEP-forced simulation achieves a better result, properly representing the phosphate maximum located around Cape Blanc, while ROM-ECHAM5 extends that maximum further north along the African coast. In this region, the modeled concentrations are clearly too high which is probably linked to a too strong upwelling of nutrients in this area. In the Northeast Atlantic, concentrations are likewise overestimated in both the ROM-NCEP and ROM-ECHAM5 simulations.

The modeled annual mean primary production shows the well-known pattern seen in observations and other models (Figure 21). Low production is found within the vast subtropical gyres. High productivity is

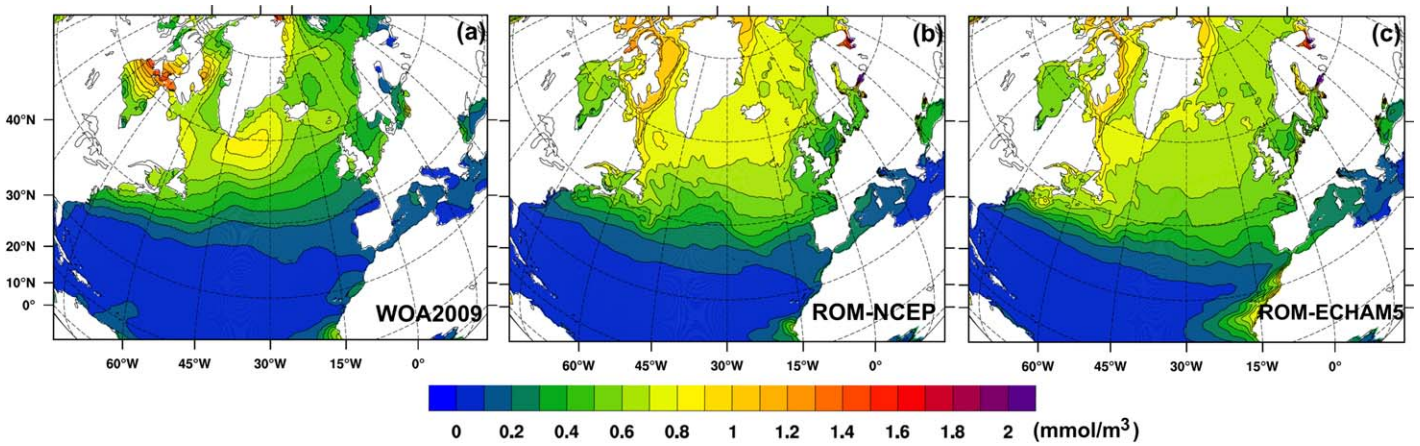

Figure 20. (a) Observed WOA2009 and modeled 1980–1999 yearly mean surface phosphate concentration. (b) ROM-NCEP and (c) ROM-ECHAM5.

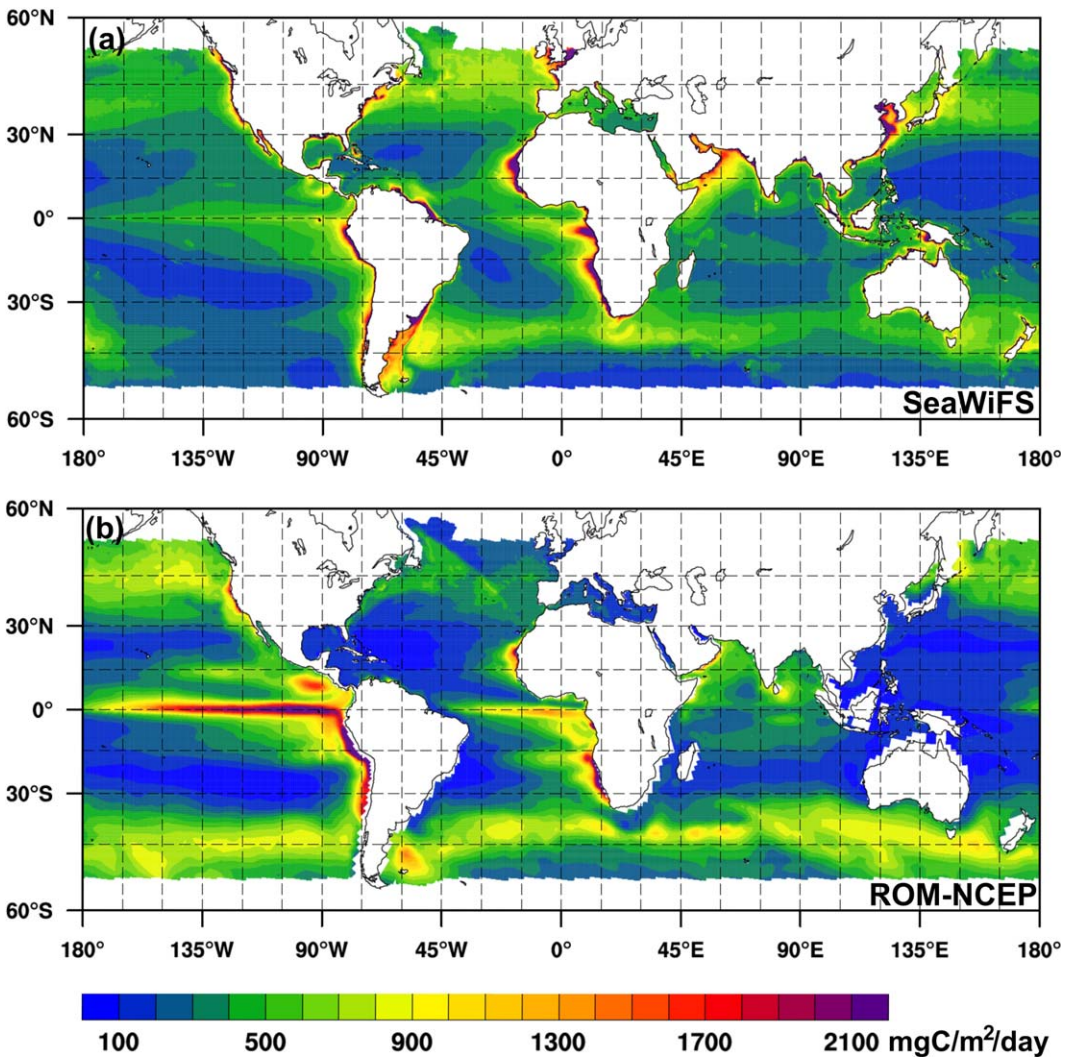

Figure 21. Vertically integrated annual mean primary production. (a) SeaWiFS [from *Behrenfeld et al.*, 2006] and (b) ROM-NCEP. Only areas with a continuous record of observations (1998–2006) are shown.

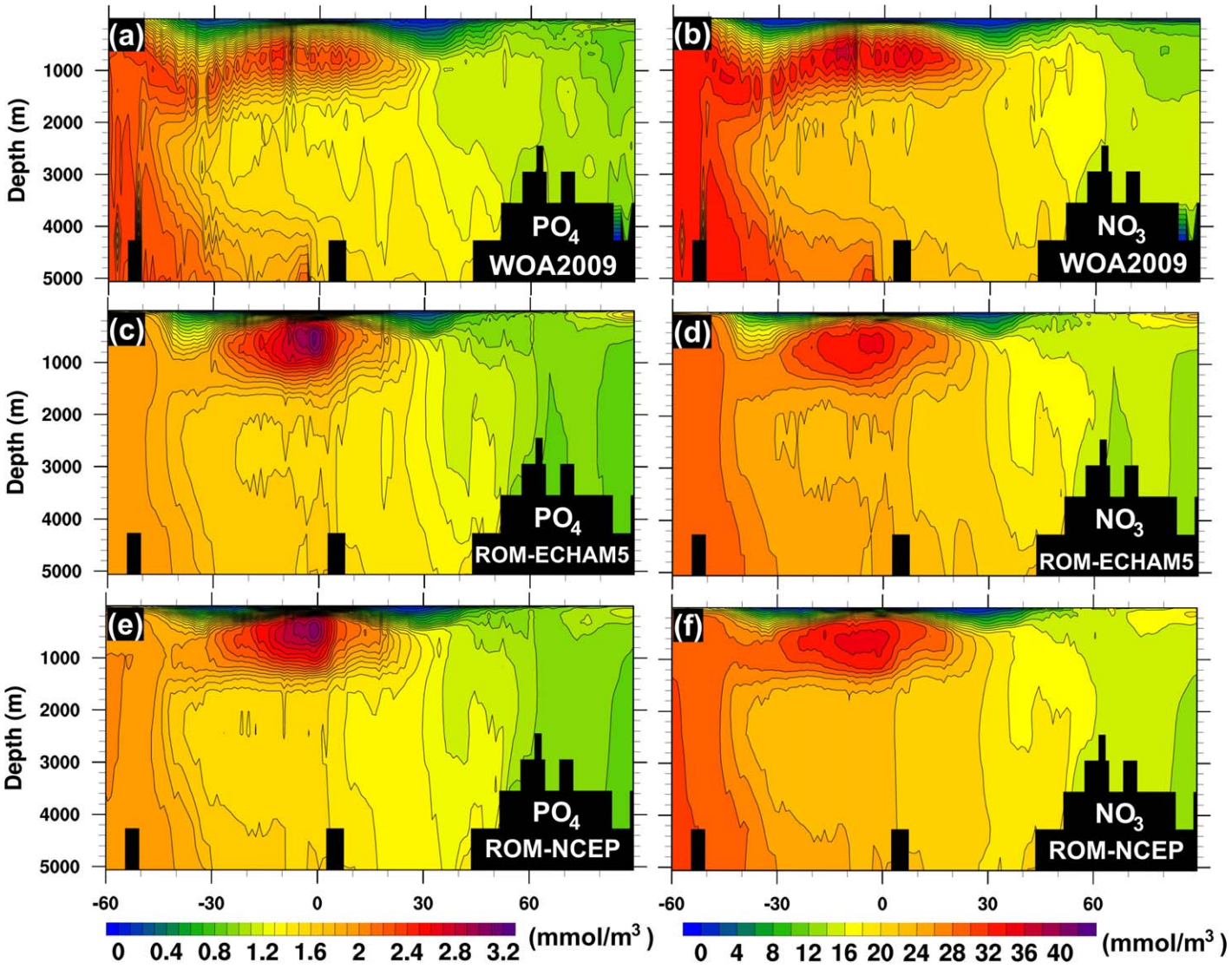

Figure 22. (a and b) Observed WOA2009 and modeled Atlantic zonally averaged phosphate and nitrate concentration. (c and d) ROM-ECHAM5 and (e and f) ROM-NCEP.

detected at high latitudes and along the tropical divergence zones in the Pacific and the Atlantic. Moreover, the high productivity associated with coastal upwelling zones like, e.g., along the western coast of Africa is reproduced. As it is known from previous studies [*Steinacher et al*., 2010], HAMOCC tends to overestimate production in the tropics and to underestimate it in the North Atlantic.

The vertical structure of nutrient distributions is shown in Figure 22. The northern North Atlantic is characterized by overall low nutrient concentration through the water column. Here nutrient depleted waters from the euphotic zone, where vigorous consumption by phytoplankton growth takes place, are transported downward by strong vertical mixing and deep convection during winter. These waters are transported via the North Atlantic Deep Water further south at depths between 2000 and 4000 m [*Maier-Reimer*, 1993, *Ilyina et al*., 2013].

Well recognized in the model simulation are also the nutrient depleted subtropical gyres which extend down to a depth of approximately 800 m due to strong wind-driven Ekman pumping (Figures 22a and 22b). The latter process is clearly underestimated in the NCEP-forced simulation (Figures 22c and 22d), as the vertical extension of the Ekman cells is clearly too shallow compared to the observations and the ECHAM-forced simulation (Figures 22e and 22f). The highest nutrient concentrations are associated with

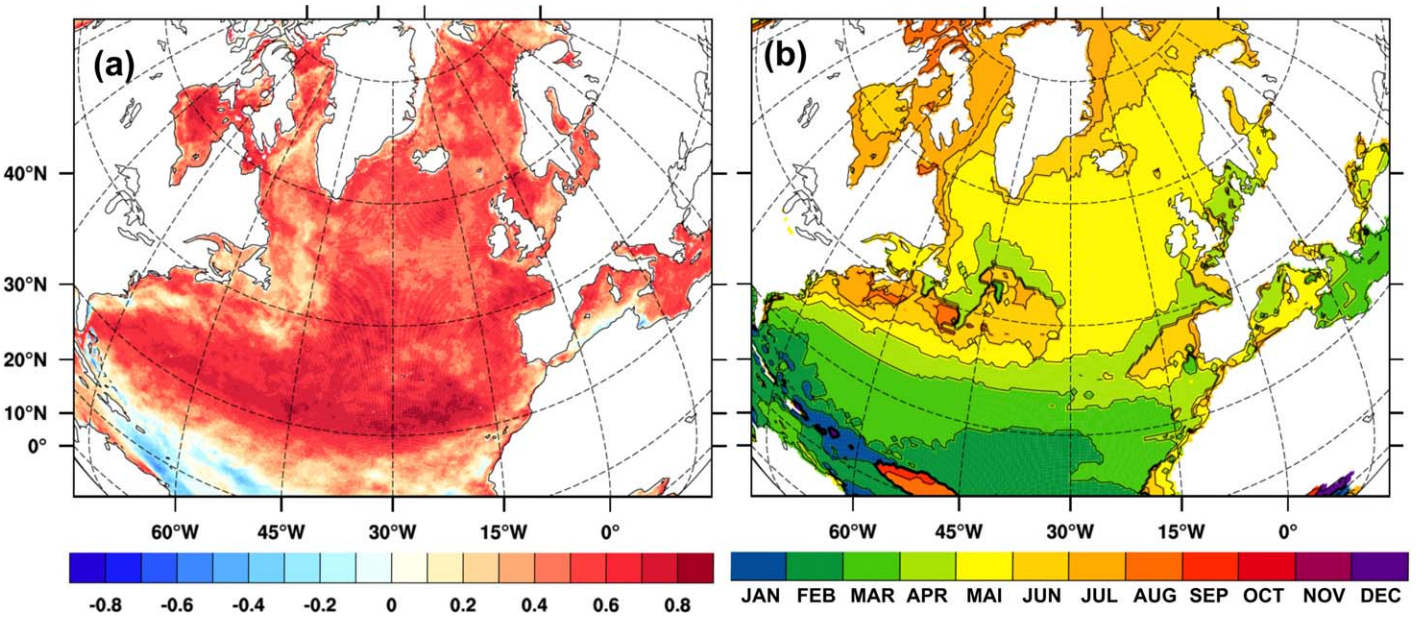

Figure 23. (a) Correlation between modeled and satellite-based estimates for net primary production (SeaWiFS) [*Behrenfeld et al*., 2006; *Behrenfeld and Falkowski*, 1997]. Displayed is the correlation of monthly mean values between 1998 and 2006. (b) Month in which the maximal production occurs (averaged over the period 1950–2000 for the ROM-ECHAM5 historical run).

Antarctic Intermediate Water at depths between 500 and 200 m. This water gains nutrients by remineralization of dead phytoplankton and zooplankton.

Integrated key parameters of the global carbon cycle compare well with values derived from the literature (Table 1). The globally integrated primary production lies in the upper range of published values while the globally integrated carbon uptake is in the lower range.

One of the greatest challenges in global biogeochemical modeling is the simulation of primary production (PP). Observational evidence is available mostly from satellites and is subject to large uncertainties. Global PP estimates from the 24 ocean color-based models range over a factor of 2 (values from less than 40 PgC/yr to more than 60 PgC/yr, [*Carr et al*., 2006]). The differences between different ocean-biogeochemistry models are in the same order of magnitude [*Steinacher et al*., 2010]. However, a high temporal correlation is identified between the ocean color-based estimated with both models, indicating that the internal variability in satellite-based estimates is reliable [*Carr et al*., 2006]. Figure 23 shows the correlation between primary production estimates of SeaWifs [*Behrenfeld et al*., 2006; *Behrenfeld and Falkowski*, 1997] and the ROM-NCEP simulation. At high latitudes, the relatively high positive correlation indicates the model's ability to reproduce the seasonal cycle of production, which relates on the limitation of the growing season due to temperature and light availability. Further south, in the realm of oligotrophic subtropical gyres, the nutrient availability becomes the dominating factor, which is mainly controlled by direct meteorological forcing (e.g., wind-driven mixing, temperature, cloudiness). The complex interplay between these processes is less well captured by the model, and the correlation with satellite-based estimates is lower (in particular south of 20°N). However, as these regions suffer from general nutrient deficiency, primary production is lowest there.

Figure 23b shows the calendar month with highest primary production. In the central and eastern Atlantic north of 50°N, the main bloom generally occurs later with increasing latitude, mainly due to a shortening and later onset of the warm season. However, the large-scale circulation cannot be neglected. Whereas the southward advection of cooler water masses via the East Greenland current clearly postpones the spring bloom, the advection of warm waters at the eastern boundary via the North Atlantic drift and the Norwegian Current tends to have the opposite effect. This leads to a large difference between the western and eastern North Atlantic in terms of the timing of the main spring bloom (more than one month). The overall high correlation north of 50°N indicates that these processes are realistically captured by the model dynamics.

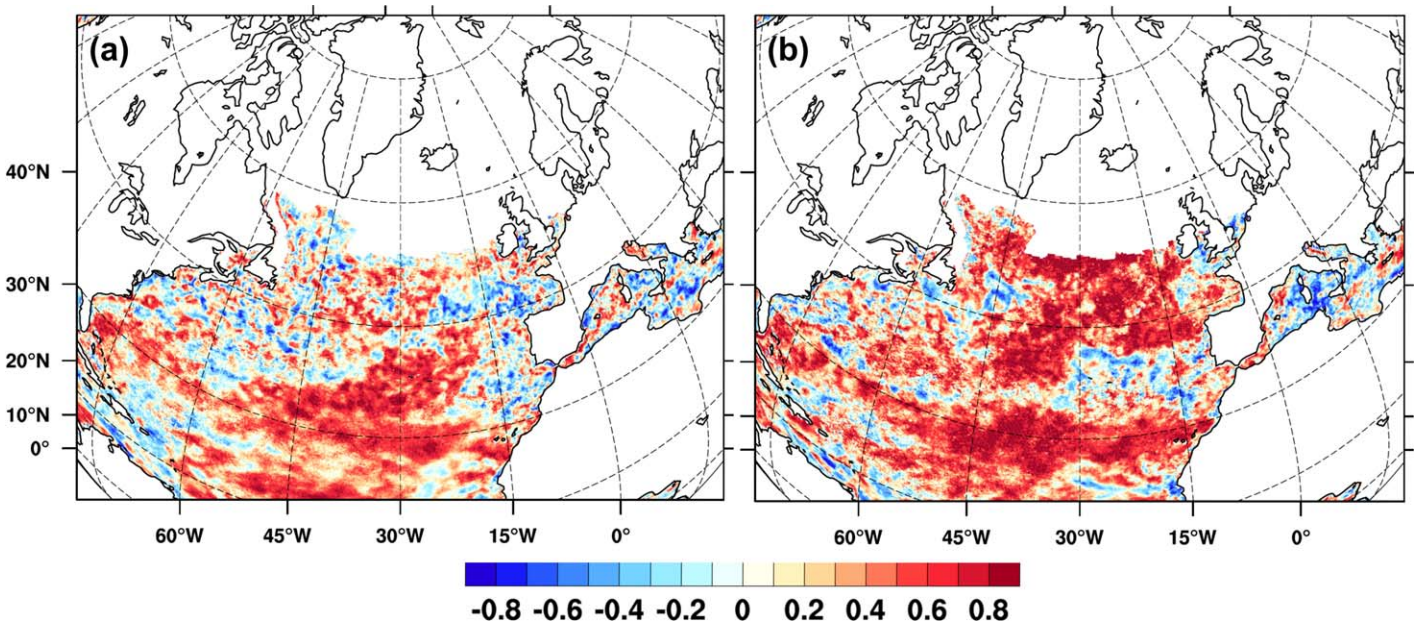

Figure 24. Correlation map between SeaWifs estimated production and ROM-NCEP simulation: (a) yearly mean production and (b) multiyear March production. The considered time frame is 1998–2006. Note: only grid points with a continuous record of ocean color data are depicted.

Pronounced meridional gradients between 30°N and 50°N along the 40°W indicate strong shifts in the timing of the production cycle on relatively small spatial scales (Figure 23). In the western part, the contributions of the cold Labrador outflow waters together with the warm and nutrient-poor waters originating from the south leads to strong gradients in temperature and nutrient concentration. Figure 23 shows generally high correlation with satellite-based estimation along this section, which indicates that the main processes of nutrient cycling and productivity are well reproduced in this area. More important, is the actual export production which determines the carbon uptake. Here the modeled export production lies well in the range of other published models (Table 1).

We have shown so far that the seasonal cycle of productivity is fairly well reproduced by the model. On the other hand, the interannual variability is of much lower amplitude than the seasonal cycle. Thus, a realistic estimation of interannual productivity variations in models must be considered as one of the most challenging issues of current global biogeochemical modeling efforts. Hence, the standard deviation of the monthly mean production is 10–15 times higher in our model than the standard deviation of yearly mean production in the North Atlantic. As free running coupled climate model simulations for the historical period cannot be directly compared to observations on a year to year basis, we use the NCEP reanalysis-forced simulation for this purpose.

Figure 24 clearly shows that the model has overall low predictive skills for annual mean variability. However, there is some significant predictive skill for interannual variations in March productivity. In order to explain the mismatch, both deficiencies in the model and in the satellite or color-based model have to be discussed. On the one hand, satellite-based estimations are subject to several uncertainties related to both input variables to the ocean color model (like chlorophyl-a, SST etc.) and deficiencies in the ocean color model itself [*Behrenfeld and Falkowski*, 1997; *Carr et al*., 2006; *Saba et al*., 2011]. On the other hand, the ROM-NCEP model deficiencies result from deficiencies in physical parameters and the circulation regime as well as deficiencies in the biogeochemical processes represented by HAMOCC. The latter constrains productivity to the presence of light and availability of nutrients. After the spring bloom, nutrient supply is the dominating factor during most of the year. Its variability is subject to smaller-scale physical processes like mesoscale eddies (which are not resolved in the model) and wind-induced mixing. The interplay of all these processes is difficult to model, but determines the nutrient supply to the euphotic zone and thus productivity. Therefore, high predictive skills cannot be expected especially in a free evolving model where ocean and atmosphere are interactively coupled and thus lack any observational/reanalysis constrain. In addition

to these physical limitations, the representation of biological processes further limits the predictive skill of the model (e.g., parameterization of the microbial loop, zooplankton grazing etc.).

Given the above, only few attempts have been undertaken so far to directly correlate productivity inferred from satellites with GCM-based estimates. *Steinacher et al*. [2010], *Seferian et al*. [2012], and *Henson et al*. [2013] restricted their investigation to spatial correlations of long-term averages, and found only weak correlations between SeaWifs productivity and four different ocean biogeochemistry GCMs. *Patara et al*. [2012], used ocean color data only for a visual comparison of the large-scale pattern in the North Pacific. *Henson et al*. [2013] provide a temporal correlation between ocean color products and modeled productivity, but restricted this to the long-term mean seasonal cycle.

Still, we found some predictive skill with respect to interannual variations of March (Figure 24b) and April productivity (not shown). During spring, nutrient saturated near-surface waters favor the onset of the spring bloom when light becomes available again. In this situation all the small-scale physical constraints on upward mixing of nutrients play only a minor role. Thus, warming of the surface water together with increasing solar radiation determines the onset and strength of the spring bloom. These two processes are strongly related to the large-scale meteorological forcing. Specifically in the North Atlantic they are closely linked to the North Atlantic Oscillation [e.g., *Hurrell and Deser*, 2009]. This large-scale mode of atmospheric circulation is generally well captured in GCMs and most likely explains the good model skill in spring.

Although the focus of this paper is mainly on the North Atlantic, the model may potentially add value for the simulation of the complex shelf environment, which has been proposed to play an important role for the global carbon cycle via carbon shelf pumping [e.g., *Tsunogai et al*., 1999]. To assess the model predictive skill in shelf regions we investigate the nutrient cycle of the North Sea as part of the NW European shelf. The North Sea is a vast shelf sea composed of a well-mixed shallow southern part influenced by anthropogenic nutrient input and a deeper northern part which is seasonally stratified with a broad connection to the North Atlantic that supplies nutrients as well, e.g., *Holt et al*. [2012] and *Gröger et al*. [2013]. The North Sea is a well-studied area (see *Emeis et al*. [2014] for an overview), with plenty of observations available for temperature, salinity and nutrients. The shelf dynamics is more complex compared to the open ocean. The biological turnover is often higher and the complex interplay between riverine nutrient input, vertical mixing, nutrient recycling, and zooplankton leads to a complex and spatially varying pattern of the seasonal nutrient cycle, especially in the southern North Sea [e.g., *Joint and Pomroy*, 1993].

We now aim to assess the model performance of the historical (ROM-ECHAM5) and NCEP (ROM-NCEP) simulation. Moreover, we investigate if there is an added value of the downscaling/regionalization. Unfortunately, the ECHAM5/MPIOM original runs were carried out without biogeochemistry, so that we have to employ the more recent run taken from the ECHAM6/MPIOM setup employed for the CMIP5 ensemble [*Ilyina et al*., 2013].

Since ocean color-based productivity estimates have been suspected to be valid for shallow ($>$250 m) and highly turbid regions [*Saba et al*., 2011], we use long-term nutrient observations from the Federal Maritime and Hydrographic Agency, Hamburg, Germany. Following the approach undertaken by *Gröger et al*. [2013], we assess how well the complex nutrient cycling in the North Sea can be reproduced by the model and if there are improvements compared to the global ECHAM6/MPIOM model. Figure 25 shows that the downscaled historical ROM-ECHAM5 and ROM-NCEP runs perform better compared to the global ECHAM6/MPIOM simulation. All model runs have biases but the downscaled runs have least RMS values (ROM-ECHAM5 = 6.05; ROM-NCEP = 6.27; ECHAM6/MPIOM = 8.83), which are in the range of internal natural variability as indicated by the standard deviation of observations (STD = 8.25). While the seasonal cycle of the global ECHAM6/MPIOM is nearly completely unrelated to the observed cycle, the downscaled runs can explain at least around 45% of the natural variability. However, all models fail to capture the full range of natural variability as indicated by the too low standard deviation (Figure 25).

There are several reasons for the low performance in nutrient cycling of the ECHAM6/MPIOM model. NO_3 concentrations are clearly too low in the southern North Sea. In the downscaled simulations phosphate is the limiting nutrient for productivity, but persistent NO_3 input from rivers leads to high concentrations in the vicinity of the coasts. The phosphate limitation near the coasts is in good agreement with observational evidence [e.g., *Skogen et al*., 2004; van *der Zee and Chou*, 2005]. The global model was driven with no additional riverine nutrient input. This explains the too low NO_3 concentrations. Furthermore, statistical

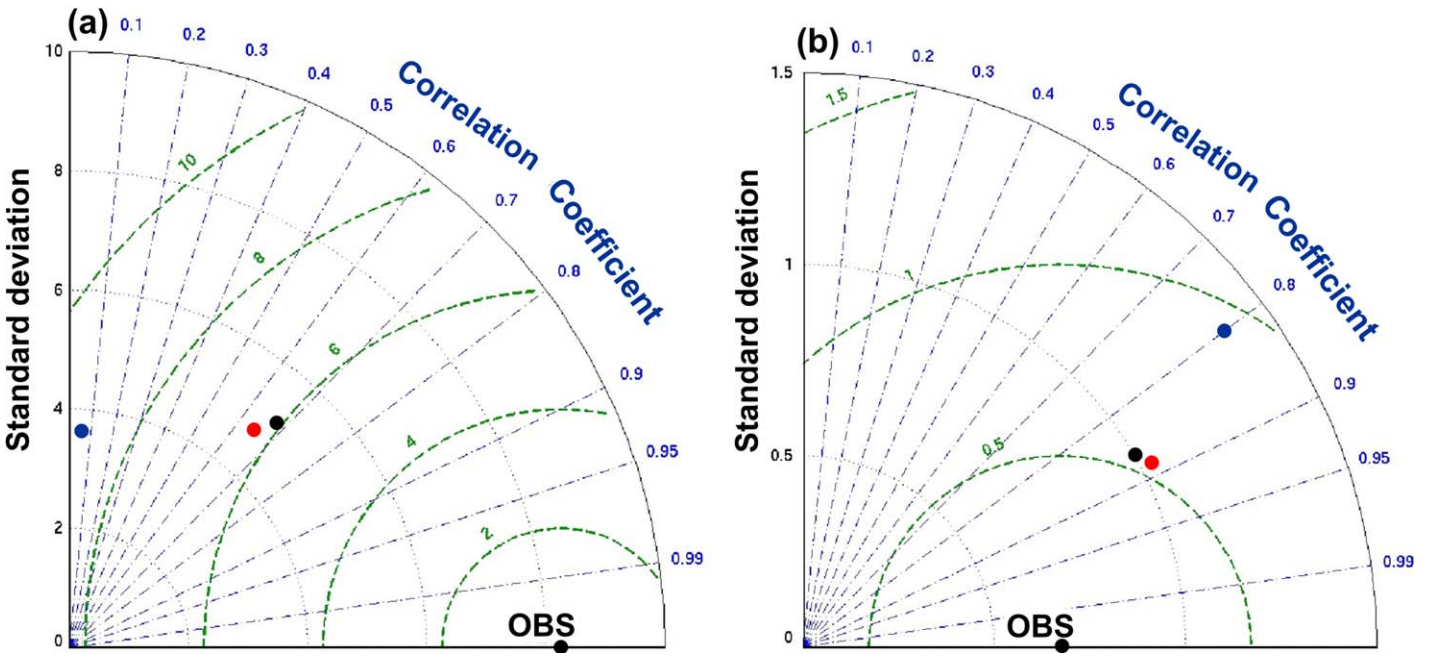

Figure 25. NO_3 analysis and salinity analysis for the North Sea. Blue: ECHAM6/MPIOM, red: ROM-NCEP, and black: ROM-ECHAM5. For the analysis of NO_3 observations were taken from Marine Environmental Database (MUDAB, http://www.marbef.org/wiki/MUDAB). In total, 2073 observations were used, distributed over the entire North Sea. About 28% originate from the upper 10 m of the water column. For salinity analysis, observations from the gridded World Ocean Atlas (2013) were employed. Analysis period is 1993–2008.

comparison with salinity data from the World Ocean Atlas (2013) indicates that all models correlate quite well with the observation-based climatology (Figure 25), but the ECHAM6/MPIOM model bias is twice as large as the one from downscaled simulations. The differences are concentrated mainly along the outflow path of water from the Baltic Sea, which is located east of the North Sea and connected to it via small straits. This outflow from the Baltic is clearly too fresh in the ECHAM6/MPIOM model, indicating problems in simulating realistically the water mass exchange (mainly related to its too coarse resolution). The properties of water masses have large influences for the phytoplankton dynamics along the coast of Norway. An important feature of the North Sea is the summer thermal stratification, which leads to a nutrient limitation of production in the upper water layers. Figure 26 shows that the downscaled ROM-ECHAM5 model captures this feature very well, when in July and August a sharp thermocline develops at around 20–25 m depth. This thermocline is not well pronounced in the ECHAM6/MPIOM simulation pointing to an overestimation of vertical mixing in the water column.

A comprehensive validation of HAMOCCs global biogeochemical fields is available from *Ilyina et al*. [2013]. More detailed validation of model's biogeochemistry with particular focus on the North Sea is available from an uncoupled model version with a somewhat lower spatial resolution [*Gröger et al*., 2013].

5. Conclusions and Discussion

A global ocean-sea ice-marine biogeochemistry coupled model (ROM) comprising the Regional atmosphere Model (REMO), the Max Planck Institute Ocean Model (MPIOM), the Hamburg Ocean Carbon Cycle (HAMOCC) model, and the Hydrological Discharge (HD) model was described and validated. All components are coupled via OASIS coupler. The regional coupled model ROM was validated against observational and reanalysis data. Historical simulations were performed using two different forcing data sets. The comparison between results obtained by ROM driven with reanalysis data (NCEP/NCAR) and with global AOGCM (ECHAM5/MPIOM) boundary conditions allowed an attribution of the sources of the model biases. For ROM-NCEP, they provide from ROM only, whereas for ROM-ECHAM5 they are additionally caused by the driving global model (ECHAM5/MPIOM) through the atmospheric boundary conditions and the ocean forcing outside the coupled area.

The ROM coupled system forced by the global AOGCM can improve the representation of key climatic variables on the regional scale by including physical processes into the MPIOM, which are not accounted for in

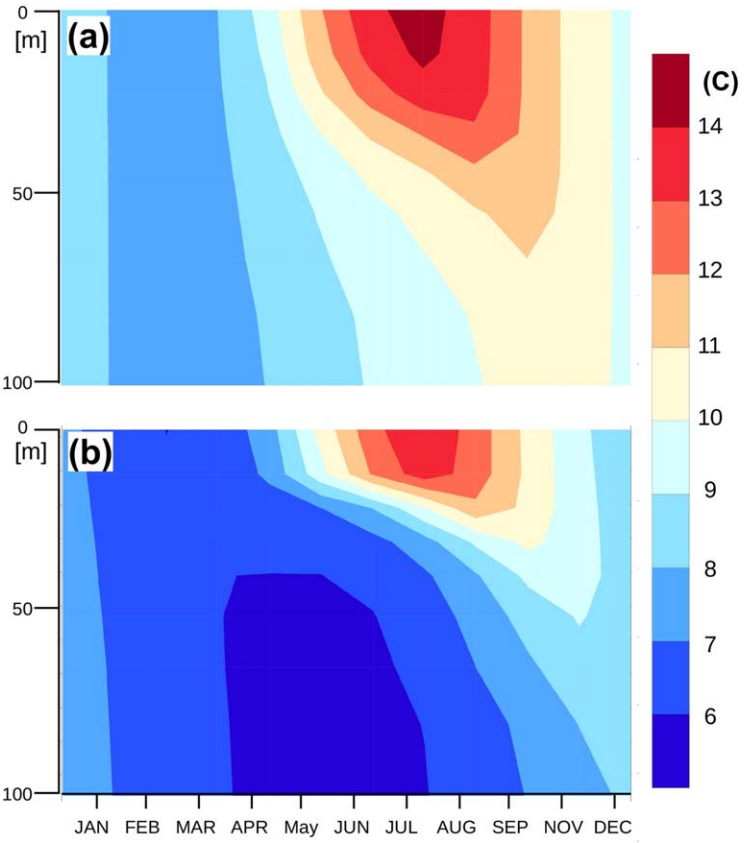

Figure 26. Yearly cycle of temperature in the northern North Sea at 0.95°E; 58.7°N obtained from (a) ECHAM6/MPIOM and (b) ROM-ECHAM5 simulations. An average is shown for the period 1980–1999.

the driving model. These improvements are mainly visible in the ocean model results. For example, the consideration of ocean tides lead to a more realistic Gulf Stream separation and an increase of the tropical water inflow into the SPG, enhancing the deep water convection in this region. Additional effect of the ocean tides on the climate is an increase of the ocean vertical mixing causing, for example, slightly warmer winter/spring (0.2–0.4 K) and slightly colder summer/autumn (−0.2 to −0.4 K) in Western Europe.

In uncoupled RCMs, the added value is mainly caused by the better representation of orography. Dynamical downscaling from GCM may be considered as a kind of "intelligent interpolation" of atmospheric fields. Recent studies have shown that there are cases when regional atmosphere-ocean climate models (RAOCMs) are capable of improving the simulation of the climate system by the driving model, e.g., *Li et al.* [2012]. The comparison between the ROM-NCEP and ROM-ECHAM5 provided evidence that the added value of the downscaling approach varies with the season, the region, and the variable/model component which is analyzed (section 4). Promising results are found, for example, for precipitation (section 4.2), which clearly document the added value of the present approach.

It is well known that biases in the driving GCM can seriously impede the potential of RCM to skillful simulations and that to a large extent RCMs reproduce the successes and failures of the global models used for driving them [e.g., *Rummukainen*, 2010], just in a higher resolution. However, the influence of the lateral boundary conditions on the RCM simulated climate depends on the relative importance of internal and external variability. It has been shown that the choice of domain size and location affects the balance between the boundary and internal model forcing in the simulations [e.g., *Diaconescu and Laprise*, 2013]. Therefore, the large-scale atmospheric circulation may be modified in coupled RAOCMs. In ROM, these changes can be even more pronounced because of the global ocean model setup [e.g., *Sein et al.*, 2014]. The differences in the modeled SPG may lead, for example, to differences in the cyclogenesis over the North Atlantic, and thus to changes in paths and intensity of extratropical cyclones over this area.

Added value of a different kind can be obtained by implementing a high-resolution ocean component for regions like the North and Baltic seas. In ECHAM5/MPIOM simulations, the ocean model is not capable to represent the exchange through the Danish Straits because of the lack of the model resolution. It leads to freshening of the Baltic Sea and finally to zero salinity in the steady model state. This does not allow a correct simulation of salinity changes in the Baltic Sea for future climate conditions, with increase of the freshwater inflow into the Baltic Sea. In contrast, our ROM model is capable to simulate the exchange between both basins and provides realistic salinity for the Baltic Sea.

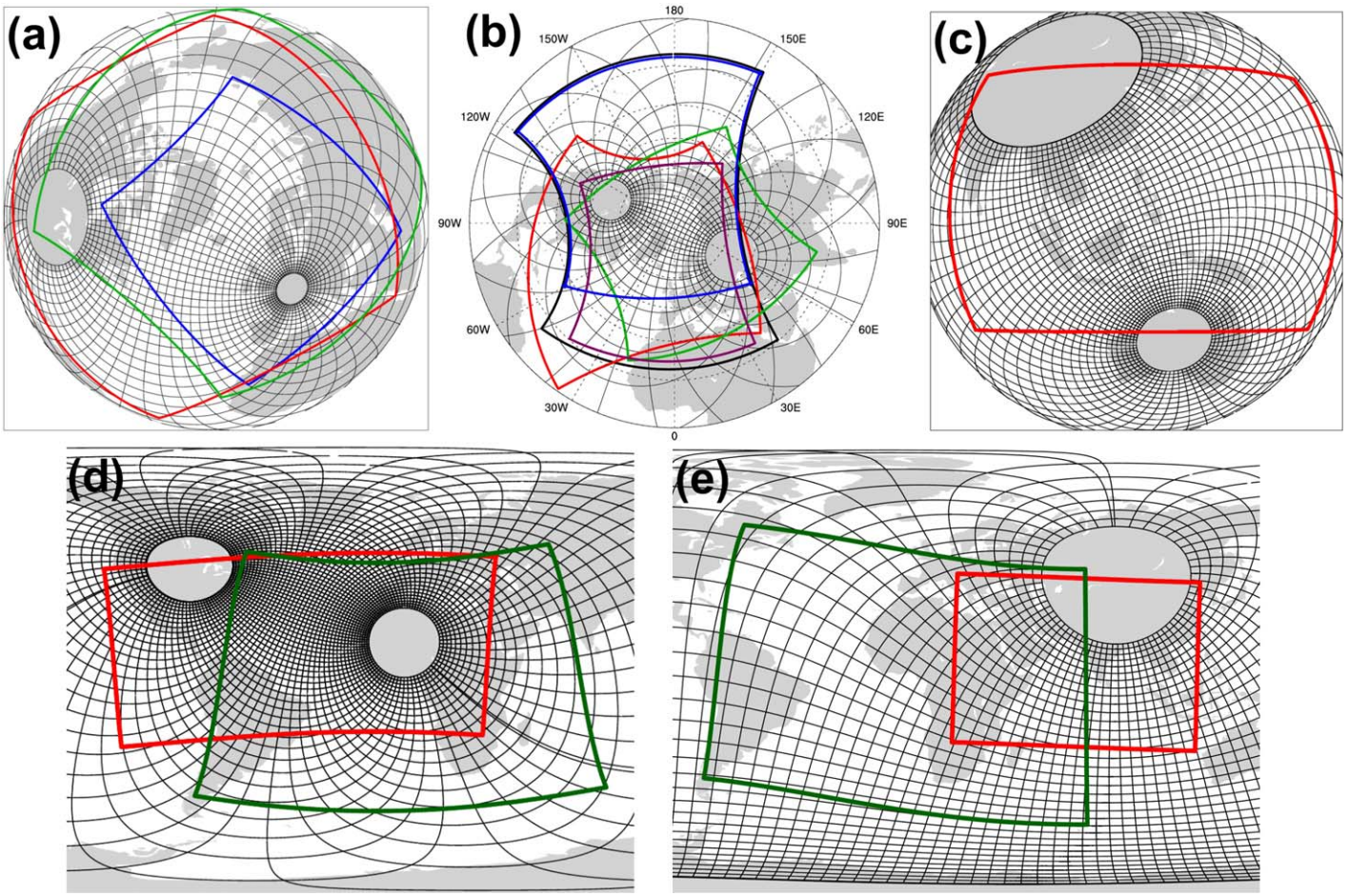

Figure 27. Various model configurations for ROM: (a) North Atlantic and Northern Europe, (b) Arctic, (c) South-East Asian, (d) West African, and (e) Indian Monsoons. Black lines—ocean model grid (every 12th grid line), colored rectangles—coupled areas.

The model has proven its ability to sufficiently reproduce the main dynamics of biogeochemical tracers. The seasonal cycle of nutrients in the high latitudes compares well with observations. Furthermore, the dynamics of primary production is reproduced well in the regions of coastal and equatorial upwelling as well as the strong seasonality of primary production in the high latitudes. Thus, the modeled globally integrated net primary production, the export production, and the total ocean carbon uptake are well within the range of published values. Accordingly, the characteristic nutrient distribution within the different deep and intermediate water masses (e.g., nutrient-poor NADW and nutrient-rich AAIW and AABW) compares well with observations.

The model also demonstrated improvements of shelf processes such as the seasonal thermal stratification and nutrient cycling in the North Sea on the NW European shelf. These processes are substantially better represented than in the global unstretched MPI-ESM CMIP5 model without downscaling. No improvements could be achieved with respect to reproducing interannual variations of yearly mean productivity in the North Atlantic. However, area-averaged interannual variations of productivity for the North Atlantic (30°W–10°E; 30°S–65°N) are positively correlated to corresponding estimates from ocean color ($r = 0.49$) and good skills could be achieved with respect to interannual variations in spring production. These are related to the strength of the first production peak of the year and probably strongly tied to the North Atlantic Oscillation.

To our best understanding, the main disadvantages of the proposed model are related to the limitation of the vertical resolution, i.e., the upper ocean model layer has to be thick enough to handle the ocean tides and underwater part of the sea ice. Another disadvantage is that the bias and internal variability generated from the global domain can influence the result in the coupled domain, making it difficult to separate the sources of bias. The apparent disadvantages in the limitation of the horizontal resolution and computational

time are questionable. The ocean component in our model allows the required refinement of the computational grid in the coupled domain, keeping there up to 70% of grid nodes. Still, it does not mean that the ocean resolution outside the coupled area is neglected. Even though the ocean model grid is coarser outside the regional atmosphere domain, it should be fine enough to reproduce general features of the global ocean circulation. This condition can also be considered as disadvantage, i.e., our ocean setups usually have larger amount of horizontal grid nodes than those in standard setups of limited area ocean model.

We conclude that the proposed model system improves many aspects of the regional climate, remarkably the ocean, while some biases persist in other model components. Therefore, there is still potential for improvement. ROM is a powerful model system that can be used to estimate possible impacts of climate change on the regional scale. In fact, the model has been developed to allow the investigation of processes in different regions of the globe (Figure 27). These include current model applications to study climate variability in the North Atlantic (Figure 27a), analyze the sensitivity of simulated regional climate to the choice of coupled domain in Arctic (Figure 27b), simulate the South-East Asia climate and its future change with the focus on typhoons generated in this region (Figure 27c), investigate the West African monsoons and hurricanes in Tropical Atlantic (Figure 27d) and study the Indian monsoon (Figure 27e). Further model applications allow improving the results of global climate models as well as understanding of the impact of relatively small-scale atmospheric process (not resolved in global AOGCMs) on present and future climate.

Acknowledgments

The authors would like to gratefully thank Ernst Maier-Reimer whose sudden death prevented him from coauthoring this manuscript. Ernst contributed significantly to this work by giving technical advice and steering the scientific model development. The authors are also thankful for his valuable help with the interpretation of simulated results of the coupled model as long as it was possible for him. The model simulations were performed at the German Climate Computing Center (DKRZ). We thank ECMWF (http://www.ecmwf.int) and NOAA (http://www.esrl.noaa.gov) for providing ERA-Interim and NCEP reanalysis data, Helmuth Haak for helping us with the MPIOM model, and Marina Tarasova and Timothy Petliar for useful discussions. The work was supported by the German Federal Ministry of Education and Research (BMBF) under the projects NORDATLANTIK (research grant 03F044E), MiKlip-DEPARTURE (research grant 01LP1129C), MiKlip-PRODEF (research grant 01LP1120A), and SPACES-AGULHAS (research grant 03G0835B). We thank the anonymous reviewers and the Editor for the constructive suggestions and critical remarks, which helped to improve the manuscript.

References

Adam, J. C., and D. P. Lettenmaier (2003), Adjustment of global gridded precipitation for systematic bias, *J. Geophys. Res.*, *108*(D9), 4257, doi:10.1029/2002JD002499.

Aldrian, E., D. Sein, D. Jacob, L. D. Gates, and R. Podzun, (2005), Modelling of Indonesian Rainfall with a Coupled Regional Model, *Clim. Dyn.*, *25*, 1–17.

Arakawa, A., and V. R. Lamb (1977), Computational design of the basic dynamical processes of the UCLA general circulation model, *Methods Comput. Phys.*, *17*, 173–265.

Artale, V., et al. (2009), An atmosphere ocean regional climate model for the Mediterranean area: Assessment of a present climate simulation, *Clim. Dyn.*, *35*, 721–740.

Avissar, R., and R. A. Pielke (1989), A parameterization of heterogeneous land surfaces for atmospheric numerical models and its impact on regional meteorology, *Mon. Weather Rev.*, *117*, 2113–2136.

Balmaseda, M. A., K. Mogensen, and A. Weaver (2013), Evaluation of the ECMWF ocean reanalysis ORAS4, *Q. J. R. Meteorol. Soc.*, *139*, 1132–1161, doi:10.1002/qj.2063.

Behrenfeld, M. J., and P. G. Falkowski (1997), Photosynthetic rates derived from satellite-based chlorophyll concentration, *Limnol. Oceanogr.*, *42*, 1–20.

Behrenfeld, M. J., R. T. O'Malley, D. A. Siegel, C. R. McClain, J. L. Sarmiento, G. C. Feldman, A. J. Milligan, P. G. Falkowski, R. M. Letelier, and E. S. Boss (2006), Climate-driven trends in contemporary ocean productivity, *Nature*, *444*, 752–755.

Bougeault, P. (1983), A non-reflective upper boundary condition for limited-height hydrostatic models, *Mon. Weather Rev.*, *111*, 420–429.

Bülow, K., et al. (2014), Comparison of three regional coupled ocean atmosphere models for the North Sea under today's and future climate conditions, *KLIWAS-27/2014*, 265 pp., Koblenz, BfG, Koblenz, Germany, doi:10.5675/Kliwas_27/2014.

Carr, M.-E., et al. (2006), A comparison of global estimates of marine primary production from ocean color, *Deep Sea Res., Part II*, *53*, 741–770, doi:10.1016/j.dsr2.2006.01.028.

Carton, J. A., and B. S. Giese (2008), A reanalysis of ocean climate using Simple Ocean Data Assimilation (SODA), *Mon. Weather Rev.*, *136*, 2999–3017.

Charnock, H. (1955), Wind stress on a water surface, *Q. J. R. Meteorol. Soc.*, *81*, 639–640.

Chen, R., G. Flerl, and C. Wunsch (2014), A description of local and nonlocal eddy-mean flow interaction in a global eddy-permitting state estimate, *J. Phys. Oceanogr.*, *44*, 2336–2352.

Cunningham, S. A., et al. (2007), Temporal variability of the Atlantic meridional overturning circulation at 26.5 degrees N, *Science*, *317*(5840), 935–938, doi:10.1126/science.1141304.

Davies, H. C. (1976), A lateral boundary formulation for multi-level prediction models, *Q. J. R. Meteorol. Soc.*, *102*, 405–418.

Dawe, J. T., and L. Thompson (2006), Effect of ocean surface currents on wind stress, heat flux, and wind power input to the ocean, *Geophys. Res. Let.*, *33*, L09604, doi:10.1029/2006GL025784.

Dee, D. P., et al. (2011), The ERA-Interim reanalysis: Configuration and performance of the data assimilation system, *Q. J. R. Meteorol. Soc.*, *137*, 553–597, doi:10.1002/qj.828.

Déqué, M., and J. P. Piedelievre (1995), Latest issue climate simulation over Europe, *Clim. Dyn.*, *11*, 321–339.

Déqué, M., D. P. Rowell, D. Lüthi, F. Giorgi, J. H. Christensen, B. Rockel, D. Jacob, E. Kjellström, M. de Castro, and B. van den Hurk (2007), An intercomparison of regional climate simulations for Europe: Assessing uncertainties in model projections, *Clim. Change*, *81*, 53–70, doi:10.1007/s10584-006-9228-x.

Diaconescu, E. P., and R. Laprise (2013), Can added value be expected in RCM-simulated large scales?, *Clim. Dyn.*, *41*, 1769–1800, doi:10.1007/s00382-012-1649-9.

Döscher R., U. Willen, C. Jones, A. Rutgersson, H. E. M. Meier, U. Hansson, and L. P. Graham (2002), The development of the regional coupled ocean-atmosphere model RCAO, *Boreal Environ. Res.*, *7*, 183–192.

Drobinski, et al. (2012), Model of the Regional Coupled Earth system (MORCE): Application to process and climate studies in vulnerable regions, *Environmental Modelling & Software*, *35*, 1–18.

Emeis, K.-C., et al. (2014), The North Sea—A shelf sea in the Anthropocene, *J. Mar. Syst.*, *141*, 18–33.

Feser, F., B. Rockel, H. von Storch, J. Winterfeldt, and M. Zahn (2011), Regional climate models add value to global model data: A review and selected examples, *Bull. Am. Meteorol. Soc.*, *92*, 1181–1192, doi:10.1175/2011BAMS3061.1.

Fouquart, Y., and B. Bonnel (1980), Computations of solar heating of the Earth's atmosphere: A new parameterization, *Beitr. Phys. Atmos.*, *53*, 35–62.
Fuchs, T., U. Schneider, and B. Rudolf (2007), *Global Precipitation Analysis Products of the GPCC, Global Precipitation Climatology Centre (GPCC)*, Deutsch. Wetterdienst, Offenbach, Germany.
Garcia, H. E., R. A. Locarnini, T. P. Boyer, J. I. Antonov, M. M. Zweng, O. K. Baranova, and D. D. Johnson (2009), *World Ocean Atlas 2009, vol. 4, Nutrients (Phosphate, Nitrate, Silicate), NOAA Atlas NESDIS 71*, edited by S. Levitus, 398 pp., U.S. Gov. Print. Off., Washington, D. C.
Gent, P. R., J. Willebrand, T. McDougall, and J. C. McWilliams (1995), Parameterizing eddy-induced tracer transports in ocean circulation models, *J. Phys. Oceanogr.*, *25*, 463–474.
Granskog, M., H. Kaartokallio, H. Kuosa, D. N. Thomas, and J. Vainio (2006), Sea ice in the Baltic Sea—A review, *Estuarine Coastal Shelf Sci.*, *70*, 145–170.
Griffies, S. M. (1998), The Gent—McWilliams skew flux, *J. Phys. Oceanogr.*, *28*, 831–841.
Gröger, M., and U. Mikolajewicz (2011), Note on the air-sea gas exchange at high temperatures, *Ocean Modell.*, *39*, 284–290, doi:10.1016/j.ocemod.2011.05.003.
Gröger, M., E. Maier-Reimer, U. Mikolajewicz, A. Moll, and D. Sein (2013), NW European shelf under climate warming: Implications for open ocean—Shelf exchange, productivity, and carbon absorption, *Biogeosciences*, *10*, 3767–3792, doi:10.5194/bg-10–3767-2013.
Hagemann, S., and L. Dümenil (1998), A parameterization of the lateral waterflow for the global scale, *Clim. Dyn.*, *14*, 17–31.
Hagemann, S., and L. Dümenil Gates (2001), Validation of the hydrological cycle of ECMWF and NCEP reanalyses using the MPI hydrological discharge model, *J. Geophys. Res.*, *106*, 1503–1510.
Hagemann, S., H. Göttel, D. Jacob, P. Lorenz, and E. Roeckner (2009), Improved regional scale processes reflected in projected hydrological changes over large European catchments, *Clim. Dyn.*, *32*(6), 767–781, doi:10.1007/s00382-008-0403-9.
Heath, M. R., A. C. Edwards, J. Pätsch, and W. R. Turell (2002), Modelling the behaviour of nutrients in the coastal waters of Scotland, *Final Rep. 10/02*, 106 pp., Fish. Res. Serv. Mar. Lab. Aberdeen, Scot. Executive Cent. Res. Unit Contract, Aberdeen, Scotland.
Heinze, C., E. Maier-Reimer, A. M. E. Winguth, and D. Archer (1999), A global oceanic sediment model for long term climate studies, *Global Biogeochem. Cycles*, *13*, 221–250.
Henson, S., H. Cole, C. Beaulieu, and A. Yool (2013), The impact of global warming on seasonality of ocean primary production, *Biogeosciences*, *10*, 4357–4369.
Hibler, W. D. (1979), A dynamic thermodynamic sea ice model, *J. Phys. Oceanogr.*, *9*, 815–846.
Holloway, G. (1987), Systematic forcing of large-scale geophysical flows by eddy-topography interaction, *J. Fluid Mech.*, *184*, 463–476.
Holloway, G. (1992), Representing topographic stress for large-scale ocean models, *J. Phys. Oceanogr.*, *22*, 1033–1046.
Holt, J., M. Butenschon, S. L. Wakelin, Y. Artioli, and J. I. Allen (2012), Oceanic controls on the primary production of the northwest European continental shelf: Model experiments under recent past conditions and a potential future scenario, *Biogeosciences*, *9*, 97–117.
Hoskins, B. J., and P. J. Valdes (1990), On the existence of storm-tracks, *J. Atmos. Sci.*, *47*, 1854–1864.
Hueging, H., K. Born, R. Haas, D. Jacob, and J. G. Pinto (2013), Regional changes in wind energy potential over Europe using regional climate model ensemble projections, *J. Appl. Meteor. Climatol.*, *52*, 903–917.
Hurrell, J. W., and C. Deser (2009), North Atlantic climate variability: The role of the North Atlantic Oscillation, *J. Mar. Syst.*, *78*(1), 28–41.
Ilyina, T., K. Six, J. Segschneider, E. Maier-Reimer, H. Li, and I. Nunez-Riboni (2013), The global ocean biogeochemistry model HAMOCC: Model architecture and performance as component of the MPI-Earth system model in different CMIP5 experimental realizations, *J. Adv. Model. Earth Syst.*, *5*, 287–315, doi: 10.1002/jame.200172013.
Jacob, D. (2001), A note to the simulation of the annual and interannual variability of the water budget over the Baltic Sea drainage basin, *Meteorol. Atmos. Phys.*, *77*(1-4), 61–73.
Jacob, D., et al. (2001), A comprehensive model intercomparison study investigating the water budget during the BALTEX-PIDCAP period, *Meteorol. Atmos. Phys.*, *77*(1-4), 19–43.
Johannessen, J. A., O. M. Johannessen, and P. Haugan (1989), Remote sensing and model simulation study in the Norwegian coastal current during the algal bloom in May 1988, *Int. J. Remote Sens.*, *10*(12), 1893–1906.
Joint, I., and A. Pomroy (1993), Phytoplankton biomass and production in the southern North Sea, *Mar. Ecol. Prog. Ser.*, *99*, 169–182.
Jungclaus, J. H., N. Keenlyside, M. Botzet, H. Haak, J.-J. Luo, M. Latif, J. Marotzke, U. Mikolajewicz, and E. Roeckner (2006), Ocean circulation and tropical variability in the coupled model ECHAM5/MPI-OM.J, *Climate*, *19*, 3952–3972.
Jungclaus, J. H., N. Fischer, H. Haak, K. Lohmann, J. Marotzke, D. Matei, U. Mikolajewicz, D. Notz, and J. S. von Storch (2013), Characteristics of the ocean simulations in MPIOM, the ocean component of the MPI-Earth system model, *J. Adv. Model. Earth Syst.*, *5*, 422–446, doi: 10.1002/jame.20023.
Kerr, R. A. (2013), Forecasting regional climate change flunks its first test, *Science*, *339*, 638–638, doi:10.1126/science.339.6120.638.
Kistler, R., et al. (2001), The NCEP/NCAR 50 year reanalysis: Monthly-means CD-ROM and documentation, *Bull. Am. Meteorol. Soc.*, *82*, 247–267.
Klemp, J. B., and D. R. Durran (1983), An upper boundary condition permitting internal gravity wave radiation in numerical mesoscale models, *Mon. Weather Rev.*, *111*, 430–444.
Le Querer, C., et al. (2009), Trends in the sources and sinks of carbon dioxide, *Nat. Geosci.*, *2*, 831–836, doi:10.1038/ngeo689.
Legutke, S., and R. Voss (1999), The Hamburg Atmosphere-Ocean Coupled Circulation Model ECHO-G, *Tech. Rep. 18*, Ger. Clim. Comput. Cent., Hamburg, Germany.
Lehmann, A., P. Lorenz, and D. Jacob (2004), Modelling the exceptional Baltic Sea inflow events in 2002–2003, *Geophys. Res. Lett.*, *31*, L21308, doi:10.1029/2004GL020830.
Levitus, S., T. P. Boyer, M. E. Conkright., T. O'Brien, J. Antonov, C. Stephens, L. Stathoplos, D. Johnson, and R. Gelfeld (1998), *World Ocean Database 1998, vol. 1, Introduction, NOAA Atlas NESDIS 18*, Ocean Clim. Lab., Natl. Oceanogr. Data Cent., U.S. Gov. Print. Off., Washington, D. C.
Li, H., M. Kanamitsu, and S.-Y. Hong (2012), California reanalysis downscaling at 10 km using an ocean-atmosphere coupled regional model system, *J. Geophys. Res.*, *117*, D12118, doi:10.1029/2011JD017372.
Li, T., and G. Q. Zhou (2010), Preliminary results of a regional air-sea coupled model over East Asia, *Chin. Sci. Bull.*, *55*, 2295–2305.
Maier-Reimer, E. (1993), Geochemical cycles in an ocean general circulation model: Preindurstrial tracer distributions, *Global Biogeochem. Cycles*, *7*, 645–677.
Maier-Reimer, E., I. Kriest, J. Segschneider, and P. Wetzel (2005), Technical description of the HAMburg Ocean Carbon Cycle model, version 5.1 (HAMOCC5.1), and of its interface to MPIOM. Reports on Earth System Science, *Max Planck Institute for Meteorol.*, Hamburg. [Available at http://edoc.mpg.de/get.epl?fid=17575&did=249293&ver=0.]
Majewski, D. (1991), The Europa modell of the Deutscher Wetterdienst, in *Seminar Proceedings ECMWF*, vol. 2, pp. 147–191, ECMWF, Reading, U. K.

Marsland, S. J., H. Haak, J. H. Jungclaus, M. Latif, and F. Roeske (2002), The Max-Planck-Institute global ocean/sea ice model with orthogonal curvilinear coordinates, *Ocean Modell.*, *5*(2), 91–126.
Metzger, E. J., et al. (2014), US Navy Operational Global Ocean and Arctic Ice Prediction Systems, *Oceanography*, *27*(3), 32–43, doi:10.5670/oceanog.2014.66.
Meybeck, M., and A. Ragu (1997), Presenting the GEMS-GLORI, a compendium of world river discharge to the oceans. Freshwater Contamination (*Proceedings of Rabat Symposium S4, April–May*), IAHS Publications, *243*, 3–14.
Mikolajewicz, U., D. Sein, D. Jacob, T. Kahl, R. Podzun, and T. Semmler (2005), Simulating Arctic sea ice variability with a coupled regional atmosphere-ocean-sea ice model, *Meteorol. Z.*, *14*(6), 793–800.
Morcrette, J.-J., and Y. Fouquart (1986), Pressure and temperature dependence of the absorption in longwave radiation parameterizations, *Beitr. Phys. Atmos.*, *59*, 455–469.
Müller, M., H. Haak, J. H. Jungclaus, J. Sündermann, and M. Thomas (2010), The effect of ocean tides on a climate model simulation, *Ocean Modell.*, *35*, 304–313.
Nicholls, J., and R. Toumi (2013), On the lake effects of the Caspian Sea, *Q. J. R. Meteorol. Soc.*, *140*, 1399–1408, doi:10.1002/qj.2222.
Nordeng, T. E. (1994), Extended versions of the convection parametrization scheme at ECMWF and their impact upon the mean climate and transient activity of the model in the tropics, *Res. Dep. Tech. Memo. 206*, ECMWF, Reading, U. K.
Orr, J., et al. (2001), Estimates of anthropogenic carbon uptake from four 3-d global ocean models, *Global Biogeochem. Cycles*, *15*, 43–60.
Patara, L., M. Vichi, and S. Masina (2012), Impacts of natural and anthropogenic climate variations on North Pacific plankton in an Earth System Model, *Ecol. Modell.*, *244*, 132–147.
Pätsch, J., and W. Kühn (2008), Nitrogen and carbon cycling in the North Sea and exchange with the North Atlantic—A model study, Part I. Nitrogen budget and fluxes, *Cont. Shelf Res.*, *28*, 767–787.
Pinto, J. G., U. Ulbrich, G. C. Leckebusch, T. Spangehl, M. Reyers, and S. Zacharias (2007), Changes in storm track and cyclone activity in three SRES ensemble experiments with the ECHAM5/MPIOM1 GCM, *Clim. Dyn.*, *29*, 195–210.
Pullen, J., J. D. Doyle, and R. P. Signell (2006), Two-way air-sea coupling: A study of the Adriatic, *Mon. Weather Rev.*, *134*, 1465–1483.
Ratnam, J. V., F. Giorgi, A. Kaginalkar, and S. Cozzini (2008), Simulation of the Indian monsoon using the RegCM3-ROMS regional coupled model, *Clim. Dyn.*, *33*, 119–139.
Rechid, D., and D. Jacob (2006), Influence of monthly varying vegetation on the simulated climate in Europe, *Meteorol. Z.*, *15*, 99–116.
Rinke, A., R. Gerdes, K. Dethloff, T. Kandlbinder, M. Karcher, F. Kauker, S. Frickenhaus, C. Köberle, and W. Hiller (2003), A case study of the anomalous Arctic sea ice conditions during 1990: Insight from coupled and uncoupled regional climate model simulations, *J. Geophys. Res.*, *108*(D9), 4275, doi:10.1029/2002JD003146.
Roeckner, E., K. Arpe, L. Bengtsson, M. Christoph, M. Claussen, L. Dümenil, M. Esch, M. Giorgetta, U. Schlese, and U. Schulzweida (1996), The Atmospheric General Circulation Model ECHAM-4: Model description and simulation of present-day-climate, *Rep. 218*, MPI für Meteorol., Hamburg, Germany.
Roeckner, E., et al. (2003), The atmospheric general circulation model ECHAM 5. PART I: Model description, *Rep. 349*, MPI für Meteorol., Hamburg, Germany.
Roeckner, E., R. Brokopf, M. Esch, M. Giorgetta, S. Hagemann, L. Kornblueh, E. Manzini, U. Schlese, and U. Schulzweida (2006), Sensitivity of simulated climate to horizontal and vertical resolution in the ECHAM5 atmosphere model, *J. Clim.*, *19*, 3771–3791.
Roeske, F. (2001), An atlas of surface fluxes based on the ECMWF re-analysis—A climatological dataset to force global ocean general circulation models, *Rep. 323*, 31 pp., MPI für Meteorol., Hamburg.
Rudolf, B., and F. Rubel (2005), Global precipitation, in *Observed Global Climate, Landolt–Boernstein: Numerical Data and Functional Relationships in Science and Technology—New Series, Group 5: Geophysics*, vol. 6, edited by M. Hantel, chap. 11, 567 pp., Springer, Berlin.
Rummukainen, M. (2010), State-of-the-art with regional climate models, *Clim. Change*, *1*(1), 82–96.
Saba, V. S., et al. (2011), An evaluation of ocean color model estimates of marine primary productivity in coastal and pelagic regions across the globe, *Biogeosciences*, *8*, 489–503.
Sanna, A., P. Lionello, and S. Gualdi (2013), Coupled atmosphere ocean climate model simulations in the Mediterranean region: Effect of a high-resolution marine model on cyclones and precipitation, *Nat. Hazards Earth Syst. Sci.*, *13*, 1567–1577, doi:10.5194/nhess-13–1567-2013.
Schaeffer, P., Y. Faugere, J. F. Legeais, A. Ollivier, T. Guinle, and N. Picot (2012), The CNES CLS11 global mean sea surface computed from 16 years of satellite altimeter data, *Mar. Geod.* (special issue, Jason-2), *35*, 3–19.
Schweiger, A., R. Lindsay, J. Zhang, M. Steele, and H. Stern (2011), Uncertainty in modeled arctic sea ice volume, *J. Geophys. Res.*, *116*, C00D06, doi:10.1029/2011JC007084.
Seferian, R., L. Bopp, M. Gehlen, J. Orr, C. Ethé, P. Cadule, O. Aumont, D. Salas-y-Melia, A. Voldoire, and G. Madec (2012), Skill assessment of three Earth system models with common marine biogeochemistry, *Clim. Dyn.*, *40*, 2549–2573, doi:10.1007/s00382-012-1362-8.
Sein, D. V., N. V. Koldunov, J. G. Pinto, and W. Cabos (2014), Sensitivity of simulated regional Arctic climate to the choice of coupled model domain, *Tellus, Ser. A*, *66*, 23966, doi:10.3402/tellusa.v66.23966.
Semmler, T., D. Jacob, K. H. Schlünzen, and R. Podzun (2002), Influence of sea ice treatment in a regional climate model on boundary layer values in the Fram Strait region, *Mon. Weather Rev.*, *132*, 985–999.
Seo, H., A. J. Miller, and J. O. Roads (2007), The scripps coupled ocean-atmosphere regional (SCOAR) model with applications in the Eastern Pacific sector, *J. Clim.*, *20*, 381–402.
She, J., P. Berg, and J. Berg (2007), Bathymetry impacts on water exchange modelling through the Danish Straits, *J. Mar. Syst.*, *65*, 450–459.
Simmons, A. J., and D. M. Burridge (1981), An energy and angular-momentum conserving vertical finite-difference scheme and hybride vertical coordinate, *Mon. Weather Rev.*, *109*, 758–766.
Skogen, M. D., H. Søiland, and E. Svendsen (2004), Effects of changing nutrient loads to the North Sea, *J. Mar. Syst.*, *46*, 23–38.
Somot, S., F. Sevault, and M. Déqué (2006), Transient climate change scenario simulation of the Mediterranean Sea for the 21st century using a high-resolution ocean circulation model, *Clim. Dyn.*, *27*, 851–879.
Somot, S., F. Sevault, M. Déqué, and M. Crépon (2008), 21st Century climate change scenario for the Mediterranean using a coupled atmosphere-ocean regional climate model, *Global Planet. Change*, *63*, 112–126.
Stacke, T., and S. Hagemann (2012), Development and validation of a global dynamical wetlands extent scheme, *Hydrol. Earth Syst. Sci.*, *16*, 2915–2933, doi:10.5194/hess-16–2915-2012.
Steele, M., R. Morley, and W. Ermold (2001), PHC: A global ocean hydrography with a high quality Arctic Ocean, *J. Clim.*, *14*, 2079–2087.
Steinacher, M., et al. (2010), Projected 21st century decrease in marine productivity: A multi-model analysis, *Biogeosciences*, *7*, 979–1005, doi:10.5194/bg-7–979-2010.
Stössel, A. (1992), The Hamburg sea-ice model, *Tech. Rep. 3*, Ger. Clim. Comput. Cent., Hamburg, Germany.

Su, J., D. V. Sein, M. Mathias, B. Mayer, K. O'Driscoll, X. Chen, U. Mikolajewicz, and T. Pohlmann (2014), Marine downscaling the global hindcast to the North Sea: A comparison of a global and a regional ocean model simulations, *Tellus, Ser. A*, *66*, 23927, doi:10.3402/tellusa.v66.23927.

Taylor, K. E., R. J. Stouffer, and G. A. Meehl (2012), An overview of CMIP5 and the experiment design, *Bull. Am. Meteorol. Soc.*, *93*, 485–498.

Thomas, M., J. Sündermann, and E. Maier-Reimer (2001), Consideration of ocean tides in an OGCM and impacts on subseasonal to decadal polar motion excitation, *Geophys. Res. Lett.*, *28*, 2457–2460.

Tibaldi, S., and F. Molteni (1990), On the operational predictability of blocking, *Tellus, Ser. A*, *42*, 343–365.

Tiedtke, M. (1989), A comprehensive mass flux scheme for cumulus parameterization in large-scale models, *Mon. Weather Rev.*, *117*, 1779–1800.

Tsunogai, S., S. Watanabe, and T. Sato (1999), Is there a continental shelf pump for the absorption of atmospheric CO_2?, *Tellus, Ser. B*, *51*, 701–712.

Valcke, S., A. Caubel, D. Declat, and L. Terray (2003), OASIS3 Ocean Atmosphere Sea Ice Soil User's Guide, *Tech. Rep. TR/CMGC/03-69*, CERFACS, Toulouse, France.

van der Zee, C., and L. Chou (2005), Seasonal cycling of phosphorus in the Southern Bight of the North Sea, *Biogeosciences*, *2*, 27–42.

Wanninkhof, R. (1992), Relationship between wind speed and gas exchange over the ocean, *J. Geophys. Res.*, *97*, 7373–7382.

Weedon, G. P., S. Gomes, P. Viterbo, W. J. Shuttleworth, E. Blyth, H. Österle, J. C. Adam, N. Bellllouin, O. Boucher, and M. Best (2011), Creation of the WATCH forcing data and its use to assess global and regional reference crop evaporation over land during the twentieth century, *J. Hydrometeorol.*, *12*, 823–848.

Wetzel, P. (2004), Interannual and decadal variability in the air-sea exchange of CO_2—A model study, PhD thesis, 127 pp., *Max-Planck Inst. for Meteorol.*, Hamburg, Germany. [Available at http://www.mpimet.mpg.de/fileadmin/publikationen/erdsystem_07.pdf.]

Zebiak, S. E., and M. A. Cane (1987), A model El Nino-Southern Oscillation, *Mon. Weather Rev.*, *115*, 2262–2278.

Zhang, J. L., and D. A. Rothrock (2003), Modeling global sea ice with a thickness and enthalpy distribution model in generalized curvilinear coordinates, *Mon. Weather Rev.*, *131*, 845–861.